# Venus: A phase equilibria approach to model surface alteration as a function of rock composition, oxygen- and sulfur fugacities

# Venus: A phase equilibria approach to model surface alteration as a function of rock composition, oxygen- and sulfur fugacities

Julia Semprich[1,2], Justin Filiberto[1], and Allan H. Treiman[1]

[1]Lunar and Planetary Institute, USRA, 3600 Bay Area Bld. Houston TX 77058, USA

[2]AstrobiologyOU, School of Environment, Earth & Ecosystem Sciences, Walton Hall, Milton Keynes, MK7 6AA, UK

Corresponding author: julia.semprich@open.ac.uk

**Abstract**

Rock alteration processes on Venus are still poorly understood due to the limited geochemical data on surface rocks and uncertainties in atmospheric compositions. We use phase equilibria calculations to constrain mineral stabilities at Venus surface conditions for different rock and gas compositions resulting in the chemical system $SiO_2$-$TiO_2$-$Al_2O_3$-FeO-MgO-CaO-$Na_2O$-$K_2O$ with C-O-H-S gas at varying $O_2$ and $S_2$ fugacities. While the low concentrations of $H_2O$ in the present-day atmosphere result in conditions, under which anhydrous mineral assemblages dominate, higher amounts of water, possibly during an earlier stage in Venus' history, could have resulted in the formation of amphibole and biotite. Even in a sulfur-free atmosphere, carbonates would be stable only in alkali-rich basalts. The presence of $SO_2$ in the atmosphere, however, causes the formation of anhydrite. The stabilities of iron oxides and sulfides are highly sensitive to gas fugacities (i.e., the composition of the atmosphere), as well as temperature. While the modeled magnetite-hematite transition is located close to conditions relevant for planetary radius, the assemblage of anhydrite + hematite ± pyrite may be stable at higher elevations if a similar range of $fO_2$ as at the lowlands is assumed. Therefore, our model agrees with pyrite proposed as cause of the high radar backscatter observed at high elevations in the northern highlands.

**Keywords:** Venus, surface; Rock alteration; Phase equilibria modeling; Iron oxides and sulfides

## 1. Introduction

Our knowledge of Venus' surface geochemistry and petrology is still limited due to the dense atmosphere and high surface temperature impeding remote sensing and *in situ* measurements of rock compositions. The most detailed geochemical constraints were obtained by the incomplete major and radioactive (U, Th, K) element data from the Venera and VEGA landers (Surkov et al., 1984, 1986), and isotopic ratios of noble gases in the lower atmosphere (von Zahn et al., 1983; Esposito et al., 1997). Further evidence for the composition of surface rocks comes from radar imaging (e.g., Masursky et al., 1980; Ivanov and Head, 2011; Tanaka et al., 1997) and near-infrared radiance measurements through atmospheric spectral windows near 1 μm, providing information that can be related to surface mineralogy and the compositional variation of surface features (e.g., Hashimoto et al., 2008; Gilmore et al., 2017). Studying rock alteration in contact with the atmosphere is hence limited to the experimental investigations of reactions in analog rocks and thermodynamic modeling. In this contribution, we use phase equilibria calculations to model phase relations of likely venusian whole-rock compositions in contact with the atmosphere at a range of conditions relevant for both modal planetary radius and higher elevations.

Radar imaging and altimetry measurements of Venus' surface area reveal a geologically complex surface comprising plains, volcanic/tectonic rises, and elevated areas composed of tectonically deformed tesserae (Ivanov and Head, 2011; Tanaka et al., 1997). Volcanic plains are the dominant landform, ~60-70% of the planet. Morphological features inferred from Magellan radar imaging (Head et al., 1992; Weitz and Basilevsky, 1993; Campbell et al., 1997; Ivanov and Head, 2011), combined with the partial *in situ* chemical analyses of Venus surface materials by Venera and VEGA landers (Surkov et al., 1984, 1986), suggest that the volcanic plains and rises are composed of basaltic rocks. Analyzed rock compositions are broadly similar to olivine tholeiites from Earth's mid-ocean ridges and alkali basalts from Earth's ocean islands (Basilevsky

et al., 1992; Kargel et al., 1993; Grimm and Hess, 1997; Fegley, 2014; Treiman, 2007; Filiberto, 2014).

In contrast, tesserae terrain covers only ~8% of the surface of Venus and consistently appears as the stratigraphically oldest material (e.g. Ivanov and Head, 1996). In the absence of *in situ* measurements and direct morphological evidence, the composition of tessera terrains remain unknown. Some constraint is provided by measurements of near-infrared surface emission of some tesserae showing values that are distinctly lower than those of the surrounding basaltic plains (Hashimoto et al., 2008; Helbert et al., 2008; Mueller et al., 2008; Basilevsky et al., 2012; Gilmore et al., 2015). This difference has been interpreted to mean that the tesserae have more felsic and less iron-rich compositions, like granitic rock (e.g. Hashimoto et al., 2008; Gilmore et al., 2015). However, 1 μm emissivity can be affected by other factors, such as grain size, surface roughness, porosity, and presence of low-emissivity weathering products that form only at higher elevations (e.g. Gilmore et al., 2017). The presence of felsic igneous rocks would either imply partial melting of hydrous materials resulting from recycled surface fluids into the Venus interior, assuming that Venus had higher water content and putative oceans early in its history (Donahue et al., 1982; Kasting and Pollack, 1983; Kumar and Taylor, 1985a; Bergh et al., 1991; Krasnopolsky, 2010; Way et al., 2016), or differentiation of basaltic melts (Hashimoto et al., 2008; Shellnutt, 2013, 2018; Filiberto, 2014).

Beyond these hints of unusual bulk composition, tesserae in northern latitudes such as Maxwell Montes and other mountain ranges around Ishtar Terra show an abrupt change in radar backscatter – above ~5 km elevation, they have very high backscatter (high reflectivity) and appear in SAR images as if they were covered with ‘snow’ (Masursky et al., 1980; Pettengill et al., 1988; Garvin et al., 1985; Klose et al., 1992; Pettengill et al., 1992; Simpson et al., 2009; Treiman et al., 2016). The cause and nature of this ‘snow,’ and the abrupt change in radar backscatter at a ‘snow line’ in the northern highlands have been debated vigorously. There is no

disagreement that the change is related to elevation, to either the decreasing pressure or temperature of the atmosphere with increasing elevation (Seiff et al., 1985). One of the first materials suggested was the semiconductor mineral pyrite ($FeS_2$) as a weathering product of basalts (Ford and Pettengill, 1983; Klose et al., 1992; Pettengill et al., 1996, 1992; Wood, 1997), although relatively large proportions of the mineral would be required to match the observed high radar reflectivity (Gilmore et al., 2017). At lower elevations and higher temperatures, a weathering product with different properties, like magnetite, is expected to be more stable and the transition from magnetite to pyrite would lead to a sharp transition in radar backscatter (a “snow line”). However, other works excluded the presence of pyrite based on thermochemical constraints (Fegley and Treiman, 1992; Fegley et al., 1995b; Fegley, 1997). A number of other semiconductor substances have been suggested as alternatives to pyrite including: metal halides and chalcogenides (Brackett et al., 1995); and “heavy metal frosts” (Pettengill et al., 1996; Schaefer and Fegley, 2004). Many of the suggested substances are either not stable at highlands surface conditions or stable at both highlands and lowlands conditions (Kohler et al., 2013, 2014). Others are exceptionally rare or unknown in terrestrial basaltic rocks (e.g. Gilmore et al., 2017).

The radar reflectivity of the northern highlands differs significantly from that observed at Ovda Regio and other near-equatorial highlands, where the backscatter coefficients rise with elevation to a maximum at 4.5 km and then drop precipitously (Klose et al., 1992; Arvidson et al., 1994; Treiman et al., 2016). This pattern can be explained by a substance that transitions from ferroelectric to dielectric such as chlorapatite (Treiman et al., 2016) or anhydrous calcium phosphates (Lazoryak et al., 2004). The absence of a semiconductor material at Ovda implies that either the atmospheric chemistry or the surface materials at Maxwell and Ovda are substantially different (Treiman et al., 2016).

Venus surface rocks have been exposed to a hot atmosphere for at least several hundred million years. The atmosphere consists mainly of $CO_2$ with minor $N_2$, and traces of noble and

chemically active gases (Fegley, 2014; Marcq et al., 2018). The concentrations of $SO_2$, CO, COS, $S_n$ and possibly other trace gases are poorly constrained in the lower 20-30 km of the atmosphere and may vary with altitude and latitude (Zolotov, 2018). At the modal planetary radius, material on the surface is exposed to temperatures of 740 K (~467 °C) and pressures of 95.6 bars (Seiff et al., 1985). At other elevations, conditions vary between 758-658 K and 110-47 bars. Thermodynamic equilibrium between near-surface gases is assumed at planetary radius (Krasnopolsky and Parshev, 1981; Fegley et al., 1997b; Krasnopolsky, 2007) but has not been confirmed by in situ measurements and latitudinal variations in gas concentration may occur (Zolotov, 2018). The lack of chemical equilibration between the major chemically active gases at higher elevations is limiting the usefulness of gas-solid type calculations of mineral stability (Zolotov, 2018, 2019).

Data from spacecraft exploration of Venus, in particular from the Venera and VEGA landers (Surkov et al., 1984, 1986), strongly suggest the chemical alteration of Venus surface rocks and fines (Zolotov, 2018, 2019). The oxidation state mainly controls which iron oxide minerals may be present on the surface of Venus. The ratio of $CO/CO_2$ in the near-surface atmosphere (Zolotov, 2015, 2018) is close to the magnetite-hematite reaction (Fegley et al., 1997b; Fegley, 2014; Zolotov, 1996, 2015), with magnetite being stable at lower oxidation state and hematite at higher. Maghemite, a common metastable oxidation product of magnetite, may also be present as a product of surface-atmosphere alteration (Gilmore et al., 2017). Reflectance spectra in visible light wavelengths suggest the presence of hematite at Venera 9 and 10 landing sites while the reflectance at the Venera 13 and 14 sites was more consistent with unaltered basalt (Pieters et al., 1986; Yamanoi et al., 2009). Venus basalts may therefore have weathered to different degrees or different alteration products. Trapping of atmospheric S in secondary minerals through alteration reactions (e.g., Zolotov, 2018) is suggested by the elevated bulk S content measured at three landing sides (Surkov et al., 1984, 1986). The Venus atmosphere

contains S-bearing gas species in S-O-C-H covering a wide range of oxidation states ($SO_2$, COS, $S_n$, $H_2S$) with the highly oxidizing $SO_2$ being the most abundant (e.g., Fegley, 2014; Marcq et al., 2018) and therefore likely the main reactant in sulfatization reactions of Ca-bearing silicates, glasses and carbonates to form anhydrite and Ca-poor silicates as suggested by thermodynamic calculations (e.g., Barsukov et al., 1986, 1982, 1982; Fegley and Treiman, 1992; Klose et al., 1992; Zolotov, 2018). However, the S/Ca ratio in the samples analyzed at the landing sites is significantly less than unity (e.g., Zolotov and Khodakovsky, 1989; Fegley and Treiman, 1992; Fegley, 2014; Zolotov, 2015), suggesting that the surface materials are not fully altered and that sulfatization reactions on Venus may be relatively slow. Estimating the degree of sulfatization of surface materials is hindered by the possible presence of secondary sulfides (e.g., Zolotov, 2018, 2019 and references therein).

Understanding the chemical alteration of surface rocks on Venus is crucial to better constrain the composition of Venus' atmosphere and surface, the composition of the highlands, and possible sources of the contrasts in radar reflectivity. Experimental studies have focused on either mineral stabilities and/or basaltic compositions as reacting solids considering $CO_2$ dominated gas mixtures predominantly at 1 bar (Zolotov, 2018 and references therein), but more recent studies have run experiments at pressures consistent with Venus' conditions (Aveline et al., 2011; Radoman-Shaw et al., 2017; Berger et al., 2019; Teffeteller et al., 2019; Port et al., 2020). A number of equilibrium chemical thermodynamic studies have considered individual gas-solid reactions and fugacity diagrams involving silicates, carbonates, Fe-oxides and phosphates and gas mixtures including $CO_2$, $H_2O$, CO, $SO_2$, COS, $H_2$, $H_2S$, HCl, and HF at temperatures relevant for Venus (e.g., Adamcik and Draper, 1963; Mueller, 1964; Lewis, 1970; Lewis and Kreimendahl, 1980; Fegley and Treiman, 1992; Nozette and Lewis, 1982; Zolotov et al., 1997; Zolotov, 2018 and references therein; Filiberto et al., 2020). This approach may not always reflect the complexity of the rocks, since reactants or products may have been consumed in reactions

that were not considered (e.g., Klose et al., 1992). Fewer studies calculated chemical equilibria in multicomponent solid-gas systems constrained by the elemental mass balances of supposed rocks and the atmosphere (e.g., Khodakovsky et al., 1979; Barsukov et al., 1982; Khodakovsky, 1982; Barsukov et al., 1986; Klose et al., 1992). This approach allows the prediction of equilibrium mineral assemblages in a chosen gas-rock system. However, solid solutions used in thermodynamic modeling have been improved since the early 90s and it is worth revisiting phase equilibria modeling for Venus.

In this work we use whole-rock compositions of tholeiitic basalt, alkali basalt, and granite, and calculate equilibrium mineral assemblages at conditions estimated at the modal planetary radius and at higher elevations. We model mineral assemblages as a function of fugacities of $H_2O$-$CO_2$ fluids and varying both oxygen and sulfur fugacities to identify phases that could have been present if Venus contained more water at an earlier stage of its formation or preserved in the subsurface. Further, we show how variations in the starting composition influence mineral stabilities and predict which phases would be expected at conditions relevant for elevated terrains and identify phases that could be associated with the contrast in radar reflectivity.

## 2. Methods

### 2.1. Model Parameters

Phase diagrams were calculated with the Gibbs free energy minimization software Perple_X 6.8.6 (Connolly, 2005) using the internally consistent thermodynamic data set of Holland and Powell (2011). The oxides MnO, $P_2O_5$, and $Cr_2O_3$ were excluded from the calculations because of their relatively low abundances and/or absence of good solid-solution models. All solid-solution models and pure phases selected for our phase equilibria calculations are listed in Table 1. The Venus atmosphere was treated as a fluid as approximation for the gas that is actually in contact with the

surface rocks, with its properties defined by the equation of state (Holland and Powell, 1991, 1998). Other gases such as $N_2$ are not expected to significantly influence surface alteration and are therefore not considered in the model. We used two different approaches to model rock alteration: (1) Calculation of phase equilibria with a $H_2O$-$CO_2$ fluid, as a function of $X_{CO_2}$ at an atmospheric pressure of 95.6 bars in the temperature range of 573-973 K to study phase stabilities at conditions relevant to an ancient water-rich environment or present-day subsurface conditions which may contain higher concentrations of $H_2O$. Oxygen fugacity is fixed by either the magnetite-hematite (MH) or the quartz-fayalite-magnetite (QFM) buffers. (2) Computation of phase equilibria as a function of $O_2$ and $S_2$ gas fugacities ($f_{O2}$ and $f_{S2}$), assuming an atmosphere dominated by $CO_2$ with 30 ppm of $H_2O$. In our model, fugacities of $O_2$ and $S_2$ are treated as independent variables, resulting in the following additional gas components: $SO_2$, CO, $H_2S$, $H_2$, and $CH_4$. Fluid/gas properties of this hybrid equation of state are computed using the Compensated-Redlich-Kwong (CORK) equation of state for $CO_2$ and $H_2O$ (Holland and Powell, 1991, 1998) and a Modified Redlich-Kwong equation of state (de Santis et al., 1974) for all components in $O_2$ and $S_2$ fugacity diagrams at atmospheric pressures of 95.6 and 50 bars, respectively.

## 2.2. Input Parameters

### *2.2.1. Starting Rock Compositions*

Three starting rock compositions (Table 2) were used for our phase equilibria calculations: (1) a synthetic tholeiitic basalt based on the Venera 14 rock analyses (Treiman, 2007) and terrestrial analogs for elements not analyzed by the lander (Filiberto, 2014), which has been used as starting composition in experimental studies (Teffeteller et al., 2019); (2) a natural alkali-rich basalt from Sverrefjell volcano, Svalbard (Skjelkvåle et al., 1989), which is chemically similar to the Venera 13 analysis (Treiman, 2007); and (3) an intraplate A-type granite from Svöfjell, southern Norway

(Auwera et al., 2003; SV1, their table 6), which was interpreted to be derived by extreme differentiation of basic magmas.

### *2.2.2. Venus surface conditions*

At the elevation of the modal planetary radius (6051.37 km), temperature and pressure are 740 K (~467 °C) and 95.6 bars (Seiff et al., 1985). Conditions at other elevations vary in the range of 758-658 K and 110-47 bars. In accordance with this data, we use 740 K and 95.6 bars for conditions at the basaltic plains and 660 K (~387 °C) at 50 bars as exemplary for high-elevation tesserae. While today's atmosphere is dominated by $CO_2$, with lesser $SO_2$, $H_2O$ and other gases (Fegley, 2014; Marcq et al., 2018), Venus' atmosphere may have contained more $H_2O$ early in its history (Way et al., 2016; Salvador et al., 2017). Hence, OH-bearing minerals may have been preserved as metastable phases or in the subsurface, where rocks are not in contact with the atmosphere. Therefore, we calculate phase stabilities for the three starting compositions as a as a function of $X_{CO_2}$ ($CO_2$/[$CO_2$+$H_2O$]) within the range of 573-973 K and a saturated $H_2O$-$CO_2$ fluid phase (i.e. assuming that a fluid/gas is always present in sufficient quantity to saturate the system in the phase). While pressure conditions are expected to vary if the atmosphere contained more $H_2O$, relatively small pressure changes (i.e. 50 bars) do not have a significant effect on phase stability. A pressure of 95.6 bars was chosen since it also covers present-day shallow subsurface conditions, where higher concentrations of water in the form of OH-bearing minerals may have been preserved.

The oxygen fugacity of the near-surface atmosphere has been derived from the calculation of chemical equilibria among atmospheric gases and lies within the range of $10^{-21.7}$ to $10^{-20}$ bars at modal planetary radius, which is indistinguishable from the MH phase boundary (Fegley et al., 1997b, 1997a; Zolotov, 1996, 2015; Fegley, 2014). The oxidation state of basalt, however, is more reduced, and ranges from near QFM on Earth to lower values on other planetary bodies (e.g.,

Herd, 2003; Schmidt et al., 2013). Based on these fugacities, we calculate phase equilibria using QFM and MH buffers for phase diagrams in $H_2O$-$CO_2$ space. Fugacity diagrams are calculated for $fO_2$ = $10^{-30}$ – $10^{-15}$ bars but we focus on phases within the range of $10^{-19}$ to $10^{-23}$ bars. The oxygen fugacity at higher elevations is not known due to a lack of gas equilibria (Krasnopolsky, 2007; Zolotov, 1996; Fegley et al., 1997a; Zolotov, 2018), which is why we assume a similar range but with larger uncertainties. Calculations including sulfur fugacity ($fS_2$) are in the range of $10^{-10}$ to $10^{-2}$ bars which cover the values of ~$10^{-5}$ bars given by Zolotov (2018), based on 0.23 ppmv of $S_2$ in the atmosphere corresponding to gas equilibrium concentrations at modal radius (Zolotov, 1996).

## 3. Results

### 3.1. Effect of $H_2O$-$CO_2$ fluid composition on phase equilibria

Figure 1 shows the calculated phase equilibria as a function of $X_{CO_2}$ at fluid saturated conditions for the three different starting rock compositions and QFM and MH $fO_2$ buffers. The molar proportion of hematite component in the ilmenite-hematite solid solution is indicated by the color coding and is an indicator of oxidization state.

Amphibole, predominantly tremolite, is the dominant hydrous phase that forms from the basaltic protolith and is stable up to $X_{CO_2}$ ~0.88 at the QFM oxidation state (Fig. 1a), and to even higher values at MH (Fig. 1b). Biotite is present only in small proportions but is stable at higher temperatures and higher $X_{CO_2}$ than amphibole. Chlorite, epidote, and white mica, mostly muscovite, are present in the lower temperature range of the phase diagrams. Calculations at MH show talc as a stable phase; it is not calculated to be stable at QFM. The stable anhydrous mineral assemblage at QFM and $CO_2$-rich conditions is orthopyroxene + clinopyroxene + feldspar +

olivine + ilmenite. At MH, a similar anhydrous assemblage is calculated, but with quartz instead of olivine. Carbonate minerals (including calcite, magnesite, and dolomite) are stable below 660 K at QFM and even lower at MH. The proportion of hematite in the hematite-ilmenite solid-solution increases with $CO_2$ and temperature for both $fO_2$ buffers but drops to nearly zero in the anhydrous assemblage of clinopyroxene + orthopyroxene + feldspar + ilmenite ± quartz ± olivine.

The altered alkali basalt is calculated to contain abundant biotite at both fugacities. Chlorite, epidote, and muscovite are stable at lower temperatures, while amphibole is absent. The anhydrous assemblage consists of clinopyroxene + plagioclase + nepheline + leucite + ilmenite, with olivine + spinel at QFM and with titanite at MH. Calcite is stable up to almost 773 K at high $X_{CO_2}$. Analogous to the alteration of tholeiitic basalt, the proportions of hematite in the hematite-ilmenite solid solution increase with higher proportions of $CO_2$ and temperature for both buffers. However, at QFM, ilmenite is not always a stable phase and is replaced by titanite.

Because of its low proportions of FeO and MgO, the mineralogy of altered granite is dominated by plagioclase, K-feldspar, and quartz. Biotite is the most stable hydrous phase at most conditions. Epidote, chlorite, and white mica are present at lower temperatures. The anhydrous mineral assemblage for QFM consists of clinopyroxene + orthopyroxene + plagioclase + K-feldspar + ilmenite + quartz. At MH, the equilibrium assemblage contains titanite instead of orthopyroxene. Carbonates are stable below temperatures of ~ 640 K.

### 3.2. Effect of $fO_2$ and $fS_2$ on phase equilibria

Phase diagrams for the compositions of the tholeiitic basalt, alkali basalt and granite as functions of $O_2$ and $S_2$ fugacities are calculated and the results for the basalt at conditions at planetary radius and higher elevations are shown in Figure 2 (phase diagrams for the alkali basalt and granite compositions are available as Supplementary Fig. 1). The compositions of the gas in equilibrium with the solid phases for both conditions are also shown in Fig. 2. Hematite and

magnetite are modeled as single phases instead of solid solutions, to show their individual stability fields. Ilmenite (without hematite) is represented by an ideal solution and spinel as a solid solution between $MgAl_2O_4$ and $FeAl_2O_4$. In an additional calculation, we explore the effect of using an ilmenite-hematite solid solution.

Figure 2a shows the calculated mineral assemblages for the tholeiite basalt protolith (Table 2) as functions of $fO_2$ and $fS_2$ at the temperature and pressure of the mean planetary radius (740 K, 95.6 bar). Fig. 2c shows the stabilities of the gas species in equilibrium with the solid phases calculated in Fig. 2a. The dominant gas phase at most fugacities is $CO_2$ while only the most oxidizing conditions considered are dominated by $SO_2$. All other gas components are present in small amounts. At oxidizing, $SO_2$-dominated and at reducing conditions, $H_2O$ is less abundant than other gases. The black box represents the most likely range of oxygen ($10^{-19}$-$10^{-23}$ bars) and sulfur ($10^{-4.2}$-$10^{-6}$ bars) fugacities, that cover the values given by Zolotov (2018) and spans the modeled MH phase boundary at an oxygen fugacity of ~$10^{-20.7}$ bars. In calculations using a solid solution of hematite and ilmenite the MH transition is shifted to $fO_2 = 10^{-23.2}$ bars, which therefore extends the stability of hematite solid solution with respect to magnetite at the mean planetary radius. Pyrite is stable at $fO_2$ ~$10^{-21}$ bars and more reducing conditions at $fS_2$ in the range of $10^{-5.2}$ – $10^{-4.1}$ bars. Pyrrhotite is not a stable phase near the mean planetary radius and requires more reducing $fO_2$ ($10^{-21.5}$ bars) and $fS_2$ below $10^{-5.2}$ bars.

As a result of an increase of $SO_2$ in the gas with oxidizing conditions in the calculated phase diagram, (Fig. 2c) anhydrite is stable starting at $fO_2 = 10^{-22.5}$ bars at $fS_2$ of $10^{-2}$ bars and $fO_2 = 10^{-20}$ bars at $fS_2$ $10^{-10}$ bars and more oxidizing conditions. Since anhydrite bonds the Ca of the system, clinopyroxene is not stable at these conditions and is replaced by other silicates such as enstatite, quartz, and cordierite. At lower temperature and pressure conditions (Fig. 2b) the transition from magnetite to hematite is shifted towards $fO_2 = 10^{-23.3}$ bars. If $fO_2$ and $fS_2$ at higher elevations are comparable to those at planetary radius, hematite is expected to be the stable

oxide at most fugacities (black rectangle, Fig 2b). Pyrite is stable at $fO_2$ ~$10^{-22}$ bars and more reducing conditions at $fS_2$ $10^{-4}$-$10^{-5.2}$ bars. Biotite is present within a small range of relatively low $fO_2$ and $fS_2$.

The phase relations of iron oxides and sulfides in the alkali basalt and granite are like those in the tholeiite and depend only on temperature and fugacities (see Fig. 1 in supplementary material). Due to differences in major oxides in the alkali basalt composition, olivine, spinel, and the feldspathoid nepheline are stable in the modeled phase diagram. Biotite is stable at most conditions except at $SO_2$ dominant and reducing conditions. Dolomite is present at high elevations and at low $fO_2$ in our model, where $SO_2$ in the gas is low (and hence conditions that are not likely for present-day Venus). In the granitic composition, calcite is a stable phase in our model at low $SO_2$. Anhydrite and silicates such as andalusite, cordierite, albite, and quartz form at $SO_2$ -rich conditions.

### 3.3. Mineral stabilities with changes in elevation

In Fig. 3 we show the modeled abundances of magnetite, hematite, pyrite, and anhydrite in the basaltic composition for three $fO_2$ and $fS_2$ pairs as a function of decreasing temperature (i.e., increasing elevation). While the pressure also decreases with elevation, it has a less significant effect on mineral stabilities and is therefore assumed at a constant value of 90 bars. At $fO_2 = 10^{-21}$ and $fS_2 = 10^{-5}$, magnetite, hematite and anhydrite are present while pyrite is not stable. The magnetite-hematite transition occurs at temperature conditions estimated for the mean planetary radius (green box in Fig. 3). If fugacities are assumed to be constant in the atmosphere, hematite and anhydrite would be the expected phases at higher elevations and pyrite would be absent. However, variations in $fO_2$ and $fS_2$ (indicated by dashed lines in Fig. 3), especially somewhat lower oxygen fugacities at $10^{-23}$, would stabilize pyrite at higher elevations.

# 4. Discussion

## 4.1. Limitations of our model

The applicability of equilibrium thermodynamic models is mainly limited by uncertainties in thermodynamic properties of minerals and their solid solutions, incomplete data of the Venus atmosphere and rock compositions and the lack of equilibration between atmospheric gases and/or at gas mineral interfaces.

Mineral stabilities in our model are influenced by uncertainties in the thermodynamic data used for minerals and solid solutions. In the case of the magnetite-hematite phase boundary, Fegley et al. (1997b) describe a large range of tabulated thermodynamic data for hematite and magnetite, which results in the variation of calculated $fO_2$ by over three orders of magnitude at Venus surface temperatures. The internally consistent thermodynamic data set (Holland and Powell, 2011) in our model is based on data for magnetite and hematite given by Robie and Hemingway (1995) and the calculated magnetite-hematite boundary in our model is therefore comparable to the results of Fegley et al. (1997b). While the temperature dependence of the thermal expansion and bulk modulus are modeled in a consistent way and thermodynamic models are in good agreement with existing experimental results, uncertainties remain due to missing calorimetric and experimental data and the use of fictive end-members used in some solid solutions (e.g., Holland and Powell, 2011).

The clinopyroxene solid solution model used in our computations does not incorporate titanium, which may result in an increased stability field and higher abundances of titanium-bearing phases such as ilmenite and rutile. Furthermore, we do not consider Mn, P, and Cr, which may shift mineral reactions and stability fields. Halogen gases such as HCl and HF, which have

been detected spectroscopically in the Venus atmosphere, are also not considered in our model but they not expected to influence mineral stabilities due to their low partial pressures (Zolotov, 2018). However, HCl can affect Na/K carbonates (Zolotov, 2018), which may not be present at surface conditions and also have not been considered in our model, but they are not expected to influence mineral stabilities die to their low partial pressures (Zolotov, 2018). However, HCL can affect Na/K carbonates (Zolotov, 2018), which may not be present at surface conditions and also have not been considered in our model. Furthermore, the gas composition does not include all species measured in the Venus atmosphere and the influence of these gas species (COS, $S_n$) are currently not modeled.

The thermodynamic data base currently does not include Na- or K-bearing sulfates and their stabilities could therefore not be explored in our model. Experiments have reported Na-Ca sulfates as alteration products (e.g., Berger et al., 2019) and we would therefore expect their presence in the $SO_2$ dominant section of the phase diagram, together with anhydrite.

Major element geochemistry from the Venera and Vega landers show large error bars compared with terrestrial analyses and are also incomplete (Surkov et al., 1984, 1986; Kargel et al., 1993; Grimm and Hess, 1997; Treiman, 2007). Variations in the whole-rock starting composition are expected to influence stabilities and proportions of minerals in our equilibrium approach. Large uncertainties are also recorded for atmospheric gas species in particular tropospheric $H_2O$, which shows significant variations and errors at altitudes from 0-15 km (Marcq et al., 2018 and references therein).

The results obtained by phase equilibria calculations assume equilibrium at all conditions considered. This implies that mineral assemblages described in this study are only present after reaching complete equilibrium with the modeled gas composition. While temperatures on Venus are sufficiently high for reactions and Venus rocks have been exposed to the atmosphere over

365 geological time scales, liquid, or supercritical water (dense solvents) are absent. In $CO_2$
366 dominated fluids, the breakdown of silicate structures may be impeded due to the very low
367 dielectric constant despite favorable Gibbs free energy of reactions. However, experimental work
368 has shown that silicate alteration occurs when $SO_2$ is present, but at different conditions than
369 estimated for present-day Venus (Delmelle et al., 2018; King et al., 2018; Palm et al., 2018;
370 Renggli and King, 2018). Oxidation of glasses is limited by the rate of chemical diffusion of cations
371 such as $Fe^{2+}$, $Ca^{2+}$, $Mg^{2+}$ and $Na^{+}$ towards the free mineral surface rather than the diffusion of
372 gases (e.g., Berger et al., 2019; Zolotov, 2018 and references therein). However, kinetic
373 constraints on solid-gas reactions are poorly constrained and require more experimental
374 evaluations at Venus conditions (Zolotov, 2018).

375 Furthermore, reaction rates vary and phases such as olivine may be more reactive than
376 others (e.g., clinopyroxene or feldspars) as suggested by the amount of S detected by surface
377 probes indicating ongoing and incomplete alteration of primary Ca-bearing minerals (except for
378 plagioclase of intermediate composition) in basalt (e.g., Barsukov et al., 1986; Zolotov, 2015) and
379 experimental studies (e.g., Radoman-Shaw et al., 2017; Berger et al., 2019; Filiberto et al., 2020).
380 The surface rocks on Venus consists of a mixture of incompletely reacted minerals from the
381 primary igneous rocks with newly formed alteration products as a result of gas-solid reactions
382 (Klose et al., 1992). While phase equilibria models cannot reflect the kinetic restrictions, they still
383 can be a helpful tool to understand, which mineral phases are likely to be expected.

384 While thermochemical equilibrium is generally assumed for near-surface conditions at
385 planetary radius (Krasnopolsky and Parshev, 1981; Krasnopolsky, 2007; Fegley et al., 1997a),
386 elevated terrains are likely exposed to gases in disequilibrium and gas compositions that differ
387 from those at modal radius (Zolotov, 1996, 2018). Due to the lack of chemical gas equilibrium,
388 $fO_2$ and fugacities of certain undetected/uncertain gases (e.g., $H_2$, $S_2$, $H_2S$) at higher elevations

cannot be evaluated by thermodynamic methods making the prediction of minerals by equilibrium calculations less reliable than for conditions at planetary radius.

Modeling equilibrium reactions is more applicable to homogeneous materials such as volcanic/impact glasses instead of rocks with large mineral grains that will alter individually at limited solid-solid diffusion (e.g., Zolotov and Volkov, 1992). Furthermore, the higher reactivity of some minerals with respect to others may lead to different alteration product than shown in our equilibrium approach.

### 4.2. Comparison to other thermodynamic models

Only a few studies used the calculations of chemical equilibria in multicomponent gas-solid type systems to study alteration processes on Venus. Khodakovsky et al. (1979) calculated the equilibrium mineralogy for a range of rock compositions, but did not include sulfur compounds and did not consider solid solutions. Below, we compare their results to our sulfur-free $H_2O$-$CO_2$ fluid calculations. In addition, Barsukov et al. (1982, 1986), Khodakovsky et al. (1982), and Klose and Zolotov (1992), used Gibbs free energy minimization models with S-bearing gases. While general comparisons are possible, each of these studies used a different approach representing atmospheric conditions, which results in variations in mineral abundances.

Khodakovsky et al. (1979) reported that their equilibrium modeling of a basalt composition (for elevations up to 5 km) yielded glaucophane, epidote, and annite as main hydrous phases with traces of chloritoid. For their sodium alkaline and potassium alkaline lavas, they predict relatively large amounts of glaucophane and phlogopite with lesser amounts of tremolite at lower temperature conditions as well as calcite, dolomite and epidote predominantly in the sodium alkaline lavas (Khodakovsky et al., 1979). In the rhyolite composition, they predict small amounts of glaucophane, chloritoid, and epidote. In our $H_2O$-$CO_2$ fluid model, amphibole is the abundant

hydrous phase in basalt, but the amphibole composition is dominated by tremolite component instead of glaucophane; glaucophane is stable only at very high pressures, > 11 kilobars at temperatures > 800 K (Corona and Jenkins, 2007; Evans, 2007). Furthermore, our results do not suggest epidote to be stable in the basalt at increasing $CO_2$. Instead, we predict talc and chlorite as hydrous phases depending on $X_{CO_2}$ and oxygen buffers in the basalt. In the granite, however, epidote is stable $X_{CO_2} < 0.8$. Biotite is mostly present in the alkali basalt and the granite. We do not report chloritoid in any composition, which is generally not a relevant phase in altered igneous rocks.

Previous energy minimization studies that include sulfur-containing species (Barsukov et al., 1982; Klose et al., 1992; Treiman and Schwenzer, 2009), report plagioclase, orthopyroxene, clinopyroxene, K-feldspar, quartz, and anhydrite at various conditions. Our results agree with those of Klose et al. (1992), with orthopyroxene and anhydrite forming at the expense of anorthite and clinopyroxene (diopside) at higher oxygen fugacities. However, they find andalusite to be the product of this reaction, whereas our model prefers cordierite in the basalt and alkali basalt compositions, and cordierite with andalusite in the granite. Barsukov et al. (1982) report small amounts of cordierite as a calculated product from their granitic protolith. Our results agree with those of Treiman and Schwenzer (2009), finding cordierite rather than andalusite to be the dominant phase when calculating phase equilibria using bulk rock compositions and solid solutions. This is also supported in results presented by Klose and Zolotov (1992), where andalusite is not a stable phase when solid solution models are considered.

All energy minimization models report the presence of iron-bearing phases such as magnetite, hematite, and pyrite. Barsukov et al. (1982) calculated the presence of either magnetite or pyrite in basalts and granites at the mean planetary radius. Klose et al. (1992), calculated that magnetite is stable rather than pyrite at mean radius conditions, but concluded that the magnetite/pyrite phase boundary varies with the redox state of the atmosphere, and

stabilizes pyrite only at higher elevations. Our model agrees with their findings supporting the stability of either magnetite, hematite, or both at planetary radius, while pyrite should be present at higher elevation where sulfur- and oxygen-fugacities may vary. Zolotov (1994) concluded that hematite solid solutions with ilmenite and geikielite are stable to lower $fO_2$ than pure hematite, which is in agreement with our results in calculations using ilmenite-hematite solid solutions. Pyrrhotite is only stable at reduced conditions according to Klose et al. (1992), and is not likely a relevant phase at present Venus conditions, which is in agreement with our results.

Klose et al. (1992) found rutile to be the Ti-bearing mineral in the basalt, which is in accordance with our results. Barsukov et al. (1982) reported either titanite or no Ti phase. We find titanite stable in the alkali basalt and granite compositions at low oxygen fugacities, but it is replaced by rutile with increasing oxidation state. Klose et al. (1992) found spinel and corundum in their basaltic composition, while Barsukov et al. (1982) reported hercynite. Neither spinel nor corundum are stable in our basaltic compositions, although spinel as solid solution is found in the alkali basalt. Olivine and nepheline are also stable in the phase diagram of the alkali basalt composition.

Neither study that considered sulfur-bearing species found that calcite would be stable at conditions of either the mean radius or higher elevations. Our results agree with these findings. However, we report the stability of dolomite in the alkali basalt, and calcite in the granite at low oxygen- and relatively high sulfur fugacities as a result of low $fSO_2/fS_2$ and therefore outside the range of anhydrite stability.

### 4.3. Comparison to experimental data

A large number of experimental works have studied gas-solid reactions at Venus conditions using either minerals or rocks as reacting solids, a variety of gas mixtures, and varying pressure-

462 temperature conditions (see Zolotov, 2018 for a review). It is beyond the scope of this paper to
463 discuss the differences in experimental conditions and results, we will focus on general
464 observations. Most studies report the formation of Fe-oxides such as magnetite and/or hematite
465 during the alteration of basaltic compositions and particularly olivine in a $CO_2$-rich environment
466 (e.g., Fegley et al., 1995a; Berger et al., 2019; Teffeteller et al., 2019). Our results agree with
467 these findings: both magnetite and hematite are thermodynamically stable on Venus and their
468 presence would depend on oxygen fugacity, which is currently poorly constrained.

469 In the presence of sulfur-bearing gases, the majority of experimental studies suggest the
470 reaction of Ca-bearing carbonates and other Ca-bearing phases such as pyroxenes to form
471 anhydrite and other Na/Ca-bearing sulfates (Fegley and Prinn, 1989; Aveline et al., 2011;
472 Radoman-Shaw et al., 2017; Berger et al., 2019). While anhydrite seems to be the most common
473 mineral in experimental studies, thenardite and glauberite also form from Na-bearing basaltic
474 glass under oxidizing conditions relevant for Venus (Berger et al., 2019) and Earth (Palm et al.,
475 2018; Renggli and King, 2018). The thermochemical databases that we used do not include Na-
476 bearing sulfates, but we predict the presence of anhydrite at most Venus conditions, which agrees
477 with experimental results. Sulfatization reactions occur within hours to days on laboratory
478 timescales and therefore would be expected to go rapidly to completion on the surface of Venus.
479 However, the chemical compositions of Venus surface materials do not show that all their Ca was
480 converted to $CaSO_4$ (e.g., Barsukov et al., 1986; Fegley and Treiman, 1992; Zolotov and Volkov,
481 1992), which suggests that anhydrite formation is relatively slow on Venus' surface (Gilmore et
482 al., 2017). Experimental data implies the migration of Ca and Na to form sulfates on the surface
483 of the solid material and possibly suppressed recrystallization of silicates below surfaces (Zolotov,
484 2018). Diffusional transport mechanics therefore seem to be rate controlling factors for the
485 formation of sulfates (Renggli and King, 2018) and reactions may slow down once the surface
486 layer has reacted with the atmosphere and the transport of elements is less feasible. Alternatively,

487 the observed S/Ca atomic rations <1 could be the result of Ca-Na plagioclase being stable with
488 respect to sulfatization (e.g., Zolotov, 2018). Our model assumes equilibrium conditions with the
489 formation of anhydrite going to completion together with cordierite and quartz as additional
490 reaction products, which are not likely to be expected on the surface if reactions are limited by
491 diffusion.

492 The stability of sulfides remains a controversial issue in experimental studies, which is
493 mainly due to significant uncertainties in abundances of $S_2$, COS, $H_2S$, and CO in the lower
494 atmosphere (Marcq et al., 2018; Johnson and Oliveira, 2019) as well as in the reaction chambers
495 and variety in gases used to assess the stability of sulfide minerals. Several experimental studies
496 found that pyrite was not stable on Venus' surface and suggested pyrrhotite might be stable
497 instead (Fegley and Treiman, 1992; Fegley, 1997; Fegley et al., 1997b; Hong and Fegley, 1998,
498 1997; Fegley et al., 1995b). In contrast, Port et al. (2016) found that pyrite could be stable. Berger
499 et al. (2019) found pyrite in an experimental run that was exposed to accidental cooling, which
500 could indicate pyrite stability at higher elevations although the concentrations of S-bearing gases
501 were uncertain in their experiments. Sulfide stability is strongly dependent on the composition of
502 the atmosphere (Zolotov, 2019), and our results confirm that even small changes in the fugacities
503 of sulfur and oxygen gas can have strong effects on the stability of pyrite. Without more precise
504 and accurate constraints on composition of Venus' atmosphere near its surface, we cannot make
505 any definite predictions about the stability of sulfides on Venus.

506 **4.4. Water-bearing phases on Venus**

507 The abundance of $H_2O$ is very low in today's atmosphere, ~ 30 ppm (Fegley, 2014; Marcq et al.,
508 2018; Zolotov, 2018) but it has been argued that Venus has lost a significant amount of water
509 throughout its history based on the high deuterium-hydrogen ratio measured in the Venusian
510 atmosphere (Donahue et al., 1982; Kumar and Taylor, 1985b; Bergh et al., 1991; Krasnopolsky,

2010). How Venus transitioned from a possibly water-bearing to a water-poor and hot atmosphere is not known and models have suggested a rapid loss (Kasting and Pollack, 1983; Kasting, 1988), a monotonic decline (Grinspoon, 1993), or a sporadic decline (Grinspoon and Bullock, 2007). In particular a sporadic decline model (Grinspoon and Bullock, 2007) could have caused more recent fluctuations in atmospheric $H_2O$ and hence resulted in the formation of OH-bearing phases. Our model shows that OH-bearing phases can form in a predominantly $CO_2$-rich environment with only a small proportion of $H_2O$ present. Experiments with added $H_2O$ do show the formation of amphibole (hornblende), chlorite, and celadonite (Berger et al., 2019), phases that are also common in our thermodynamic models. While the present surface conditions would likely have resulted in the dehydration of these phases, they may have been present during an earlier stage of Venus or still exist in the subsurface that is not in contact with the atmosphere (Zolotov, 2018). However, decomposition experiments have shown that tremolite could survive over geological time scales under Venus surface conditions (Johnson and Fegley, 2000, 2003a, 2003b).

### 4.5. Radar anomalies at higher elevations

The nature of the high radar backscatter material at higher elevations is still a matter of debate. Here, we only discuss the relevance of our model for the radar anomalies in the northern latitude since we have not considered ferroelectric materials that can explain the radar behavior at Ovda Regio and other equatorial highlands (Treiman et al., 2016). A number of materials have been suggested as cause for the high radar backscatter at Maxwell Montes, including semiconductor minerals such as pyrite (Ford and Pettengill, 1983; Klose et al., 1992; Pettengill et al., 1992, 1996; Wood, 1997), although a relatively large amount would be required to match the permittivity values (Gilmore et al., 2017). The stability of pyrite on Venus' highlands, however, was questioned since the atmosphere was considered too oxidizing (Fegley et al., 1997b) and other substances

were suggested including perovskite (Fegley et al., 1992), chalcogenide compounds (Brackett et al., 1995), and 'heavy metal frosts' (Pettengill et al., 1996; Schaefer and Fegley, 2004). The elements in most of these compounds are rare in the solar system, and particularly so in igneous rocks (e.g., Bi, Te, Nb), and would therefore require significant enrichment processes to be present in abundances that match the radar properties (Treiman et al., 2016; Gilmore et al., 2017). Furthermore, experimental studies have shown that many of these are not stable at highland surface conditions, or are stable at all Venus conditions and can therefore not explain the changes in radar reflectivity with elevation (Kohler et al., 2012, 2013, 2014; Guandique et al., 2014; Port et al., 2020).

Results of our work are consistent with earlier suggestions that pyrite could be stable at higher elevation. Furthermore, at specific oxygen- and sulfur fugacities, pyrite transitions to hematite at higher elevations (Fig. 3), which could provide an alternative explanation for the sudden drop in radar brightness in certain regions. Therefore, we suggest that pyrite could cause the high radar backscatter material on Maxwell Montes and possibly other high elevation areas.

## 5. Conclusions

We used calculations of equilibrium mineral assemblages in multi-component gas-solid systems open with respect to $CO_2$, $O_2$, and $S_2$ gases to model rock-atmosphere reactions at Venus surface conditions for whole rock compositions ranging from basaltic to granitic. In sulfur-free model runs with $CO_2$-$H_2O$ fluids that could possibly reflect an early, water-rich Venus ore present-day subsurface, amphibole and biotite are the dominant Oh-bearing minerals but are replaced by H-free assemblages at high $X_{CO_2}$. Calcite may occur at lower temperature in the alkali-rich basalt. At high $fSO_2$, however, Ca-carbonates are not stable at conditions of planetary radius and instead replaced by anhydrite. The stabilities of Fe-oxides and sulfides are very sensitive to variations in atmospheric composition and fugacities that are currently not well known for the surface of Venus.

However, even when considering a larger range of oxygen and sulfur fugacities, our work is consistent with previous findings that conditions at the modal planetary radius are close to the magnetite-hematite transition for all considered rock types, while the assemblage of hematite + anhydrite ± pyrite may be more likely at lower temperatures (and pressures). The presence of pyrite may therefore be responsible for the observed radar brightness of some mountain tops, negating the need for highly uncommon phases such as chalcogenides and 'heavy metal frosts'.

**Acknowledgements:** This work was partially funded by NASA grant SSW#80NSSC17K0766. M. Zolotov and G. Berger are thanked for their detailed reviews that greatly improved an earlier version of this manuscript. O. Aharonson is thanked for editorial handling. This is LPI contribution number 2348.

## References

Adamcik, J.A., Draper, A.L., 1963. The temperature dependence of the Urey equilibrium and the problem of the carbon dioxide content of the atmosphere of Venus. Planetary and Space Science 11, 1303–1307. https://doi.org/10.1016/0032-0633(63)90235-6

Arvidson, R.E., Brackett, R.A., Shepard, M.K., Izenberg, N.R., Fegley, B., Plaut, J.J., 1994. Microwave Signatures and Surface Properties of Ovda Regio and Surroundings, Venus. Icarus 112, 171–186. https://doi.org/10.1006/icar.1994.1176

Auwera, J.V., Bogaerts, M., Liégeois, J.-P., Demaiffe, D., Wilmart, E., Bolle, O., Duchesne, J.C., 2003. Derivation of the 1.0–0.9 Ga ferro-potassic A-type granitoids of southern Norway by extreme differentiation from basic magmas. Precambrian Research, Origin and Evolution of Precambrian Anorogenic Magmatism 124, 107–148. https://doi.org/10.1016/S0301-9268(03)00084-6

Aveline, D.C., Abbey, W.J., Choukroun, M., Treiman, A.H., Dyar, M.D., Smrekar, S.E., Feldman, S.M., 2011. Rock and mineral weathering experiments under model Venus conditions. Presented at the 42nd Lunar and Planetary Science Conference. Abstract #2165.

Barsukov, V.L., Borunov, S.P., Volkov, V.P., Dorofeeva, V.A., Zolotov, M.I., 1986. Analysis of the mineral composition of soil at the landing sites of the Venera-13, Venera-14, and Vega-2 landers on the basis of thermodynamic calculations. Akademiia Nauk SSSR Doklady (in Russian) 287, 415.

Barsukov, V.L., Volkov, V.P., Khodakovsky, I.L., 1982. The crust of Venus: Theoretical models of chemical and mineral composition. Journal of Geophysical Research: Solid Earth 87, A3–A9. https://doi.org/10.1029/JB087iS01p000A3

591 Basilevsky, A.T., Nikolaeva, O.V., Weitz, C.M., 1992. Geology of the Venera 8 landing site region from
592 Magellan data: Morphological and geochemical considerations. Journal of Geophysical
593 Research: Planets 16315–16335. https://doi.org/10.1029/92JE01557@10.1002/(ISSN)2169-
594 9100.MAGELLAN1
595 Basilevsky, A.T., Shalygin, E.V., Titov, D.V., Markiewicz, W.J., Scholten, F., Roatsch, Th., Kreslavsky, M.A.,
596 Moroz, L.V., Ignatiev, N.I., Fiethe, B., Osterloh, B., Michalik, H., 2012. Geologic interpretation of
597 the near-infrared images of the surface taken by the Venus Monitoring Camera, Venus Express.
598 Icarus, Advances in Venus Science 217, 434–450. https://doi.org/10.1016/j.icarus.2011.11.003
599 Berger, G., Cathala, A., Fabre, S., Borisova, A.Y., Pages, A., Aigouy, T., Esvan, J., Pinet, P., 2019.
600 Experimental exploration of volcanic rocks-atmosphere interaction under Venus surface
601 conditions. Icarus 329, 8–23. https://doi.org/10.1016/j.icarus.2019.03.033
602 Bergh, C.D., Bézard, B., Owen, T., Crisp, D., Maillard, J.-P., Lutz, B.L., 1991. Deuterium on Venus:
603 Observations from Earth. Science 251, 547–549. https://doi.org/10.1126/science.251.4993.547
604 Brackett, R.A., Fegley, B., Arvidson, R.E., 1995. Volatile transport on Venus and implications for surface
605 geochemistry and geology. Journal of Geophysical Research: Planets 100, 1553–1563.
606 https://doi.org/10.1029/94JE02708
607 Campbell, B.A., Arvidson, R.E., Shepard, M.K., Brackett, R.A., 1997. Remote sensing and surface
608 properties, in: Bougher, S.W., Hunten, D.M., Phillips, R.J. (Eds.), Venus II, Space Science Series.
609 University of Arizona Press, Tucson, pp. 503–526.
610 Connolly, J.A.D., 2005. Computation of phase equilibria by linear programming: A tool for geodynamic
611 modeling and its application to subduction zone decarbonation. EPSL 236, 524–541.
612 https://doi.org/10.1016/j.epsl.2005.04.033
613 Corona, J.C., Jenkins, D.M., 2007. An experimental investigation of the reaction: glaucophane + 2 quartz
614 = 2 albite + talc. European Journal of Mineralogy 147–158. https://doi.org/10.1127/0935-
615 1221/2007/0019-1719
616 de Santis, R., Breedveld, G.J.F., Prausnitz, J.M., 1974. Thermodynamic properties of aqueous gas
617 mixtures at advanced pressures. Ind. Eng. Chem. Proc. Des. Dev. 13, 374–377.
618 https://doi.org/10.1021/i260052a013
619 Delmelle, P., Wadsworth, F.B., Maters, E.C., Ayris, P.M., 2018. High temperature reactions between
620 gases and ash particles in volcanic eruption plumes. Reviews in Mineralogy and Geochemistry
621 84, 285–308. https://doi.org/10.2138/rmg.2018.84.8
622 Donahue, T.M., Hoffman, J.H., Hodges, R.R., Watson, A.J., 1982. Venus was wet: A measurement of the
623 ratio of deuterium to hydrogen. Science 216, 630–633.
624 https://doi.org/10.1126/science.216.4546.630
625 Esposito, L.W., Bertaux, J.-L., Krasnopolsky, V.A., Moroz, V.I., Zasova, L.V., 1997. Chemistry of the lower
626 atmosphere and clouds, in: Bougher, S.W., Hunten, D.M., Phillips, R.J. (Eds.), Venus II: Geology,
627 Geophysics, Atmosphere, and Solar Wind Environment. University of Arizona Press, Tucson, p.
628 415.
629 Evans, B.W., 2007. The synthesis and stability of some end-member amphiboles. Reviews in Mineralogy
630 and Geochemistry 67, 261–286. https://doi.org/10.2138/rmg.2007.67.7
631 Fegley, B., 2014. Venus, in: Holland, H.D., Turekian, K.K. (Eds.), Treatise on Geochemistry (Second
632 Edition). Pergamon, Oxford, pp. 127–148. https://doi.org/10.1016/B978-0-08-095975-7.00122-4
633 Fegley, B., 1997. Why pyrite is unstable on the surface of Venus. Icarus 128, 474–479.
634 https://doi.org/10.1006/icar.1997.5744
635 Fegley, B., Klingelhöfer, G., Brackett, R.A., Izenberg, N., Kremser, D.T., Lodders, K., 1995a. Basalt
636 oxidation and the formation of hematite on the surface of Venus. Icarus 118, 373–383.
637 https://doi.org/10.1006/icar.1995.1197

638 Fegley, B., Klingelhöfer, G., Lodders, K., Widemann, T., 1997a. Geochemistry of surface-atmosphere
639 interactions on Venus, in: Venus II: Geology, Geophysics, Atmosphere, and Solar Wind
640 Environment. pp. 591–636.
641 Fegley, B., Lodders, K., Treiman, A.H., Klingelhöfer, G., 1995b. The rate of pyrite decomposition on the
642 surface of Venus. Icarus 115, 159–180. https://doi.org/10.1006/icar.1995.1086
643 Fegley, B., Prinn, R.G., 1989. Estimation of the rate of volcanism on Venus from reaction rate
644 measurements. Nature 337, 55–58. https://doi.org/10.1038/337055a0
645 Fegley, B., Treiman, A.H., 1992. Chemistry of atmosphere-surface interactions on Venus and Mars.
646 Washington DC American Geophysical Union Geophysical Monograph Series 66, 7–71.
647 https://doi.org/10.1029/GM066p0007
648 Fegley, B., Treiman, A.H., Sharpton, V.L., 1992. Venus surface mineralogy: Observational and theoretical
649 constraints, in: Lunar and Planetary Science Conference Proceedings, Volume 22. pp. 3–19.
650 Fegley, B., Zolotov, M.Yu., Lodders, K., 1997b. The oxidation state of the lower atmosphere and surface
651 of Venus. Icarus 125, 416–439. https://doi.org/10.1006/icar.1996.5628
652 Filiberto, J., 2014. Magmatic diversity on Venus: Constraints from terrestrial analog crystallization
653 experiments. Icarus 231, 131–136. https://doi.org/10.1016/j.icarus.2013.12.003
654 Filiberto, J., Trang, D., Treiman, A.H., Gilmore, M.S., 2020. Present-day volcanism on Venus as evidenced
655 from weathering rates of olivine. Science Advances 6, eaax7445.
656 https://doi.org/10.1126/sciadv.aax7445
657 Ford, P.G., Pettengill, G.H., 1983. Venus: Global surface radio emissivity. Science 220, 1379–1381.
658 https://doi.org/10.1126/science.220.4604.1379
659 Garvin, J.B., Head, J.W., Pettengill, G.H., Zisk, S.H., 1985. Venus global radar reflectivity and correlations
660 with elevation. Journal of Geophysical Research: Solid Earth 90, 6859–6871.
661 https://doi.org/10.1029/JB090iB08p06859
662 Gilmore, M.S., Mueller, N., Helbert, J., 2015. VIRTIS emissivity of Alpha Regio, Venus, with implications
663 for tessera composition. Icarus 254, 350–361. https://doi.org/10.1016/j.icarus.2015.04.008
664 Gilmore, M.S., Treiman, A.H., Helbert, J., Smrekar, S., 2017. Venus surface composition constrained by
665 observation and experiment. Space Sci Rev 212, 1511–1540. https://doi.org/10.1007/s11214-
666 017-0370-8
667 Grimm, R.E., Hess, P.C., 1997. The Crust of Venus, in: Bougher, S.W., Hunten, D.M., Phillips, R.J. (Eds.),
668 Venus II: Geology, Geophysics, Atmosphere, and Solar Wind Environment, Space Science Series.
669 University of Arizona Press, Tucson, pp. 1205–1244.
670 Grinspoon, D.H., 1993. Implications of the high D/H ratio for the sources of water in Venus' atmosphere.
671 Nature 363, 428–431. https://doi.org/10.1038/363428a0
672 Grinspoon, D.H., Bullock, M.A., 2007. Astrobiology and Venus Exploration, in: Esposito, L.W., Stofan,
673 E.R., Cravens, T.E. (Eds.), Exploring Venus as a Terrestrial Planet, Geophysical Monograph Series
674 176. American Geophysical Union, Washington, D. C., pp. 191–206.
675 https://doi.org/10.1029/176GM12
676 Guandique, J., Kohler, E., Chevrier, V., 2014. Stability of metallic minerals under venusian surface
677 temperatures: Investigating the potential source of radar anomalies. Presented at the 45th
678 Lunar and Planetary Science Conference. Abstract #2391.
679 Hashimoto, G.L., Roos-Serote, M., Sugita, S., Gilmore, M.S., Kamp, L.W., Carlson, R.W., Baines, K.H.,
680 2008. Felsic highland crust on Venus suggested by Galileo Near-Infrared Mapping Spectrometer
681 data. Journal of Geophysical Research: Planets 113, E00B24.
682 https://doi.org/10.1029/2008JE003134
683 Head, J.W., Crumpler, L.S., Aubele, J.C., Guest, J.E., Saunders, R.S., 1992. Venus volcanism: Classification
684 of volcanic features and structures, associations, and global distribution from Magellan data.
685 Journal of Geophysical Research: Planets 97, 13153–13197. https://doi.org/10.1029/92JE01273

686 Helbert, J., Müller, N., Kostama, P., Marinangeli, L., Piccioni, G., Drossart, P., 2008. Surface brightness
687 variations seen by VIRTIS on Venus Express and implications for the evolution of the Lada Terra
688 region, Venus. Geophysical Research Letters 35. https://doi.org/10.1029/2008GL033609
689 Herd, C.D.K., 2003. The oxygen fugacity of olivine-phyric martian basalts and the components within the
690 mantle and crust of Mars. Meteoritics & Planetary Science 38, 1793–1805.
691 https://doi.org/10.1111/j.1945-5100.2003.tb00015.x
692 Holland, T., Powell, R., 1991. A Compensated-Redlich-Kwong (CORK) equation for volumes and fugacities
693 of CO2 and H2O in the range 1 bar to 50 kbar and 100–1600°C. Contributions to Mineralogy and
694 Petrology 109, 265–273. https://doi.org/10.1007/BF00306484
695 Holland, T.J.B., Powell, R., 2011. An improved and extended internally consistent thermodynamic
696 dataset for phases of petrological interest, involving a new equation of state for solids. J.
697 Metamorph. Geol. 29, 333–383. https://doi.org/j.1525-1314.2010.00923.x
698 Holland, T.J.B., Powell, R., 1998. An internally consistent thermodynamic data set for phases of
699 petrological interest. Journal of Metamorphic Geology 16, 309–343.
700 Hong, Y., Fegley, B., 1998. The sulfur vapor pressure over pyrite on the surface of Venus. Planetary and
701 Space Science 46, 683–690. https://doi.org/10.1016/S0032-0633(97)00127-X
702 Hong, Y., Fegley, B., 1997. The kinetics and mechanism of pyrite thermal decomposition. Berichte der
703 Bunsengesellschaft für physikalische Chemie 101, 1870–1881.
704 https://doi.org/10.1002/bbpc.19971011212
705 Ivanov, M.A., Head, J.W., 2011. Global geological map of Venus. Planetary and Space Science, Exploring
706 Phobos 59, 1559–1600. https://doi.org/10.1016/j.pss.2011.07.008
707 Ivanov, M.A., Head, J.W., 1996. Tessera terrain on Venus: A survey of the global distribution,
708 characteristics, and relation to surrounding units from Magellan data. Journal of Geophysical
709 Research: Planets 101, 14861–14908. https://doi.org/10.1029/96JE01245
710 Johnson, N.M., Fegley, B., 2003a. Tremolite decomposition on Venus II. Products, kinetics, and
711 mechanism. Icarus 164, 317–333. https://doi.org/10.1016/S0019-1035(03)00102-7
712 Johnson, N.M., Fegley, B., 2003b. Longevity of fluorine-bearing tremolite on Venus. Icarus 165, 340–348.
713 https://doi.org/10.1016/S0019-1035(03)00212-4
714 Johnson, N.M., Fegley, B., 2000. Water on Venus: New insights from tremolite decomposition. Icarus
715 146, 301–306. https://doi.org/10.1006/icar.2000.6392
716 Johnson, N.M., Oliveira, M.R.R. de, 2019. Venus atmospheric composition in situ data: A compilation.
717 Earth and Space Science 6, 1299–1318. https://doi.org/10.1029/2018EA000536
718 Kargel, J.S., Komatsu, G., Baker, V.R., Strom, R.G., 1993. The volcanology of Venera and VEGA landing
719 sites and the geochemistry of Venus. Icarus 103, 253–275.
720 https://doi.org/10.1006/icar.1993.1069
721 Kasting, J.F., 1988. Runaway and moist greenhouse atmospheres and the evolution of Earth and Venus.
722 Icarus 74, 472–494. https://doi.org/10.1016/0019-1035(88)90116-9
723 Kasting, J.F., Pollack, J.B., 1983. Loss of water from Venus. I. Hydrodynamic escape of hydrogen. Icarus
724 53, 479–508. https://doi.org/10.1016/0019-1035(83)90212-9
725 Khodakovsky, I.L., 1982. Atmosphere-surface interactions on Venus and implications for atmospheric
726 evolution. Planetary and Space Science 30, 803–817. https://doi.org/10.1016/0032-
727 0633(82)90113-1
728 Khodakovsky, I.L., Volkov, V.P., Sidorov, Yu.I., Borisov, M.V., 1979. Venus: Preliminary prediction of the
729 mineral composition of surface rocks. Icarus 39, 352–363. https://doi.org/10.1016/0019-
730 1035(79)90146-5
731 King, P.L., Wheeler, V.M., Renggli, C.J., Palm, A.B., Wilson, S.A., Harrison, A.L., Morgan, B., Nekvasil, H.,
732 Troitzsch, U., Mernagh, T., Yue, L., Bayon, A., DiFrancesco, N.J., Baile, R., Kreider, P., Lipiński, W.,
733 2018. Gas–solid reactions: Theory, experiments and case studies relevant to earth and planetary

734 processes. Reviews in Mineralogy and Geochemistry 84, 1–56.
735 https://doi.org/10.2138/rmg.2018.84.1
736 Klose, K.B., Wood, J.A., Hashimoto, A., 1992. Mineral equilibria and the high radar reflectivity of Venus
737 mountaintops. Journal of Geophysical Research: Planets 97, 16353–16369.
738 https://doi.org/10.1029/92JE01865
739 Klose, K.B., Zolotov, M.Y., 1992. Chemical weathering of evolved igneous rocks on Venus, in: Abstracts of
740 the Lunar and Planetary Science Conference. Volume 23. p. 699.
741 Kohler, E., Chevrier, V.F., Gavin, P., Johnson, N., 2013. Experimental stability of tellurium and its
742 implications for the venusian radar anomalies. Presented at the 44th Lunar and Planetary
743 Science Conference. Abstract #2951.
744 Kohler, E., Chevrier, V.F., Johnson, N., Craig, P., Lacy, C., 2014. Proposed radar-reflective minerals tested
745 under Venus surface and atmospheric conditions. Presented at the 45th Lunar and Planetary
746 Science Conference. Abstract #2321.
747 Kohler, E., Gavin, P., Chevrier, V.F., Johnson, N., 2012. Experimental investigation into the radar
748 anomalies on the surface of Venus. Presented at the 43rd Lunar and Planetary Science
749 Conference. Abstract #2749.
750 Krasnopolsky, V.A., 2010. Spatially-resolved high-resolution spectroscopy of Venus 2. Variations of HDO,
751 OCS, and SO2 at the cloud tops. Icarus 209, 314–322.
752 https://doi.org/10.1016/j.icarus.2010.05.008
753 Krasnopolsky, V.A., 2007. Chemical kinetic model for the lower atmosphere of Venus. Icarus 191, 25–37.
754 https://doi.org/10.1016/j.icarus.2007.04.028
755 Krasnopolsky, V.A., Parshev, V.A., 1981. Chemical composition of the atmosphere of Venus. Nature 292,
756 610–613. https://doi.org/10.1038/292610a0
757 Kumar, S., Taylor, H.A., 1985a. Deuterium on Venus: Model comparisons with pioneer Venus
758 observations of the predawn bulge ionosphere. Icarus 62, 494–504.
759 https://doi.org/10.1016/0019-1035(85)90189-7
760 Kumar, S., Taylor, H.A., 1985b. Deuterium on Venus: Model comparisons with pioneer Venus
761 observations of the predawn bulge ionosphere. Icarus 62, 494–504.
762 https://doi.org/10.1016/0019-1035(85)90189-7
763 Lazoryak, B.I., Morozov, V.A., Belik, A.A., Stefanovich, S.Yu., Grebenev, V.V., Leonidov, I.A., Mitberg, E.B.,
764 Davydov, S.A., Lebedev, O.I., Van Tendeloo, G., 2004. Ferroelectric phase transition in the
765 whitlockite-type Ca9Fe(PO4)7; crystal structure of the paraelectric phase at 923 K. Solid State
766 Sciences 6, 185–195. https://doi.org/10.1016/j.solidstatesciences.2003.12.007
767 Lewis, J.S., 1970. Venus: Atmospheric and lithospheric composition. Earth and Planetary Science Letters
768 10, 73–80. https://doi.org/10.1016/0012-821X(70)90066-X
769 Lewis, J.S., Kreimendahl, F.A., 1980. Oxidation state of the atmosphere and crust of Venus from pioneer
770 Venus results. Icarus 42, 330–337. https://doi.org/10.1016/0019-1035(80)90098-6
771 Marcq, E., Mills, F.P., Parkinson, C.D., Vandaele, A.C., 2018. Composition and chemistry of the neutral
772 atmosphere of Venus. Space Sci Rev 214, 10. https://doi.org/10.1007/s11214-017-0438-5
773 Masursky, H., Eliason, E., Ford, P.G., McGill, G.E., Pettengill, G.H., Schaber, G.G., Schubert, G., 1980.
774 Pioneer Venus Radar results: Geology from images and altimetry. Journal of Geophysical
775 Research: Space Physics 85, 8232–8260. https://doi.org/10.1029/JA085iA13p08232
776 Mueller, N., Helbert, J., Hashimoto, G.L., Tsang, C.C.C., Erard, S., Piccioni, G., Drossart, P., 2008. Venus
777 surface thermal emission at 1 μm in VIRTIS imaging observations: Evidence for variation of crust
778 and mantle differentiation conditions. Journal of Geophysical Research: Planets 113.
779 https://doi.org/10.1029/2008JE003118
780 Mueller, R.F., 1964. A chemical model for the lower atmosphere of Venus. Icarus 3, 285–298.
781 https://doi.org/10.1016/0019-1035(64)90037-5

Nozette, S., Lewis, J.S., 1982. Venus: Chemical weathering of igneous rocks and buffering of atmospheric composition. Science 216, 181–183. https://doi.org/10.1126/science.216.4542.181
Palm, A.B., King, P.L., Renggli, C.J., Hervig, R.L., Dalby, K.N., Herring, A., Mernagh, T.P., Eggins, S.M., Troitzsch, U., Beeching, L., Kinsley, L., Guagliardo, P., 2018. Unravelling the consequences of SO2–basalt reactions for geochemical fractionation and mineral formation. Reviews in Mineralogy and Geochemistry 84, 257–283. https://doi.org/10.2138/rmg.2018.84.7
Pettengill, G.H., Ford, P.G., Chapman, B.D., 1988. Venus: Surface electromagnetic properties. Journal of Geophysical Research: Solid Earth 93, 14881–14892. https://doi.org/10.1029/JB093iB12p14881
Pettengill, G.H., Ford, P.G., Simpson, R.A., 1996. Electrical properties of the Venus surface from bistatic radar observations. Science 272, 1628–1631. https://doi.org/10.1126/science.272.5268.1628
Pettengill, G.H., Ford, P.G., Wilt, R.J., 1992. Venus surface radiothermal emission as observed by Magellan. Journal of Geophysical Research: Planets 97, 13091–13102. https://doi.org/10.1029/92JE01356
Pieters, C.M., Head, J.W., Pratt, S., Patterson, W., Garvin, J., Barsukov, V.L., Basilevsky, A.T., Khodakovsky, I.L., Selivanov, A.S., Panfilov, A.S., Gektin, Y.M., Narayeva, Y.M., 1986. The color of the surface of Venus. Science 234, 1379–1383. https://doi.org/10.1126/science.234.4782.1379
Port, S.T., Chevrier, V.F., Kohler, E., 2020. Investigation into the radar anomaly on Venus: The effect of Venus conditions on bismuth, tellurium, and sulfur mixtures. Icarus 336, 113432. https://doi.org/10.1016/j.icarus.2019.113432
Port, S.T., Kohler, E., Craig, P.I., Chevrier, V.F., 2016. Stability of pyrite under Venusian surface conditions. Presented at the 47th Lunar and Planetary Science Conference. Abstract #2144.
Radoman-Shaw, B.G., Harvey, R.P., Costa, G.C.C., Jacobson, N.S., Avishai, A., Nakley, L.M., 2017. The stability of calcium silicates and calcium carbonate on the surface of Venus. Presented at the 48th Lunar and Planetary Science Conference. Abstract #2701.
Renggli, C.J., King, P.L., 2018. SO2 gas reactions with silicate glasses. Reviews in Mineralogy and Geochemistry 84, 229–255. https://doi.org/10.2138/rmg.2018.84.6
Robie, R.A., Hemingway, B.S., 1995. Thermodynamic properties of minerals and related substances at 298.15 K and 1 bar (10^5 pascals) pressure and at higher temperatures (USGS Numbered Series No. 2131).
Salvador, A., Massol, H., Davaille, A., Marcq, E., Sarda, P., Chassefière, E., 2017. The relative influence of H2O and CO2 on the primitive surface conditions and evolution of rocky planets. Journal of Geophysical Research: Planets 122, 1458–1486. https://doi.org/10.1002/2017JE005286
Schaefer, L., Fegley, B., 2004. Heavy metal frost on Venus. Icarus 168, 215–219. https://doi.org/10.1016/j.icarus.2003.11.023
Schmidt, M.E., Schrader, C.M., McCoy, T.J., 2013. The primary fO2 of basalts examined by the Spirit rover in Gusev Crater, Mars: Evidence for multiple redox states in the martian interior. Earth and Planetary Science Letters 384, 198–208. https://doi.org/10.1016/j.epsl.2013.10.005
Seiff, A., Schofield, J.T., Kliore, A.J., Taylor, F.W., Limaye, S.S., Revercomb, H.E., Sromovsky, L.A., Kerzhanovich, V.V., Moroz, V.I., Marov, M.Ya., 1985. Models of the structure of the atmosphere of Venus from the surface to 100 kilometers altitude. Advances in Space Research 5, 3–58. https://doi.org/10.1016/0273-1177(85)90197-8
Shellnutt, J.G., 2018. Derivation of intermediate to silicic magma from the basalt analyzed at the Vega 2 landing site, Venus. PLOS ONE 13, e0194155. https://doi.org/10.1371/journal.pone.0194155
Shellnutt, J.G., 2013. Petrological modeling of basaltic rocks from Venus: A case for the presence of silicic rocks. Journal of Geophysical Research: Planets 118, 1350–1364. https://doi.org/10.1002/jgre.20094

828 Simpson, R.A., Tyler, G.L., Häusler, B., Mattei, R., Pätzold, M., 2009. Venus Express bistatic radar: High-
829 elevation anomalous reflectivity. Journal of Geophysical Research: Planets 114.
830 https://doi.org/10.1029/2008JE003156
831 Skjelkvåle, B.-L., Amundsen, H.E.F., O'Reilly, S.Y., Griffin, W.L., Gjelsvik, T., 1989. A primitive alkali
832 basaltic stratovolcano and associated eruptive centres, Northwestern Spitsbergen: Volcanology
833 and tectonic significance. Journal of Volcanology and Geothermal Research 37, 1–19.
834 https://doi.org/10.1016/0377-0273(89)90110-8
835 Surkov, Y.A., Barsukov, V.L., Moskalyeva, L.P., Kharyukova, V.P., Kemurdzhian, A.L., 1984. New data on
836 the composition, structure, and properties of Venus rock obtained by Venera 13 and Venera 14.
837 Journal of Geophysical Research: Solid Earth 89, B393–B402.
838 https://doi.org/10.1029/JB089iS02p0B393
839 Surkov, Y.A., Moskalyova, L.P., Kharyukova, V.P., Dudin, A.D., Smirnov, G.G., Zaitseva, S.Y., 1986. Venus
840 rock composition at the Vega 2 Landing Site. Journal of Geophysical Research: Solid Earth 91,
841 E215–E218. https://doi.org/10.1029/JB091iB13p0E215
842 Tanaka, K.L., Senske, D.A., Price, M., Kirk, R.L., 1997. Physiography, geologic/geomorphic mapping, and
843 stratigraphy of Venus, in: Bougher, S.W., Hunten, D.M., Phillips, R.J. (Eds.), Venus II. University of
844 Arizona Press, pp. 667–694.
845 Teffeteller, H., McCanta, M., Cherniak, D., Treiman, A.H., Filiberto, J., Rutherford, M.J., Johnson, N.,
846 2019. Experimental study of the alteration of basalt on the surface of Venus. Presented at the
847 50th Lunar and Planetary Science Conference. Abstract #1858.
848 Treiman, A.H., 2007. Geochemistry of Venus' surface: current limitations as future opportunities, in:
849 Esposito, L.W., Stofan, E.R., Cravens, T.E. (Eds.), Exploring Venus as a Terrestrial Planet,
850 Geophysical Monograph Series 176. American Geophysical Union, Washington, D. C., pp. 7–22.
851 Treiman, A.H., Harrington, E., Sharpton, V., 2016. Venus' radar-bright highlands: Different signatures and
852 materials on Ovda Regio and on Maxwell Montes. Icarus 280, 172–182.
853 https://doi.org/10.1016/j.icarus.2016.07.001
854 Treiman, A.H., Schwenzer, S.P., 2009. Basalt-atmosphere interaction on Venus: Preliminary results on
855 weathering of minerals and bulk rock. Presented at the Venus Geochemistry: Progress,
856 Prospects, and New Missions Workshop.
857 von Zahn, U., Kumar, S., Niemann, R., Prinn, R., 1983. Composition of the Venus atmosphere, in: Hunten,
858 D.M., Colin, L., Donahue, T.M., Moroz, V.I. (Eds.), Venus. University of Arizona Press, Tucson, p.
859 299.
860 Way, M.J., Genio, A.D.D., Kiang, N.Y., Sohl, L.E., Grinspoon, D.H., Aleinov, I., Kelley, M., Clune, T., 2016.
861 Was Venus the first habitable world of our solar system? Geophysical Research Letters 43,
862 8376–8383. https://doi.org/10.1002/2016GL069790
863 Weitz, C.M., Basilevsky, A.T., 1993. Magellan observations of the Venera and Vega landing site regions.
864 Journal of Geophysical Research: Planets 98, 17069–17097. https://doi.org/10.1029/93JE01776
865 Wood, J.A., 1997. Rock weathering on the surface of Venus, in: Bougher, S.W., Hunten, D.M., Phillips,
866 R.J. (Eds.), Venus II: Geology, Geophysics, Atmosphere and Solar Wind Environment. University
867 of Arizona Press, Tucson, pp. 637–664.
868 Yamanoi, Y., Nakashima, S., Katsura, M., 2009. Temperature dependence of reflectance spectra and
869 color values of hematite by in situ, high-temperature visible micro-spectroscopy. American
870 Mineralogist 94, 90–97. https://doi.org/10.2138/am.2009.2779
871 Zolotov, M., 2019. Chemical weathering on Venus. Oxford Research Encyclopedia of Planetary Science.
872 https://doi.org/10.1093/acrefore/9780190647926.013.146
873 Zolotov, M., 1996. A model for the thermal equilibrium of the surface venusian atmosphere. GEOCHEM.
874 INT. 33, 80–100.

Zolotov, M., Volkov, V.P., 1992. Chemical processes on the planetary surface. Venus geology, geochemistry and geophysics 177–199.
Zolotov, M.Y., 1994. Phase relations in the Fe-Ti-Mg-O oxide system and hematite stability at the condition of Venus' surface, in: 25th Lunar and Planetary Science Conferece. Abract #1571.
Zolotov, M.Y., Khodakovsky, I.L., 1989. Exogenic processes, in: Barsukov, V.L., Volkov, V.P. (Eds.), The Planet Venus: Atmosphere, Surface, Interior Structure. Nauka, Moscow, pp. 262–290.
Zolotov, M.Yu., 2018. Gas–solid interactions on Venus and other solar system bodies. Reviews in Mineralogy and Geochemistry 84, 351–392. https://doi.org/10.2138/rmg.2018.84.10
Zolotov, M.Yu., 2015. 10.12 - Solid Planet–Atmosphere Interactions, in: Schubert, G. (Ed.), Treatise on Geophysics (Second Edition). Elsevier, Oxford, pp. 411–427. https://doi.org/10.1016/B978-0-444-53802-4.00182-2
Zolotov, M.Yu., Fegley, B., Lodders, K., 1997. Hydrous silicates and water on Venus. Icarus 130, 475–494. https://doi.org/10.1006/icar.1997.5838

**Table 1:** Solution models and pure phases used in phase equilibria calculations.

| Mineral or solid solution, abbreviation used in Perple_X | Formula of main components | Abbreviation | Reference |
|---|---|---|---|
| **Amphiboles** | | | |
| Clinoamphibole, cAmph (G) | *tremolite:* $Ca_2Mg_5Si_8O_{22}(OH)_2$<br>*Fe-tremolite:* $Ca_2Fe_5Si_8O_{22}(OH)_2$<br>*grunerite:* $Fe_7Si_8O_{22}(OH)_2$<br>*cummingtonite:* $Mg_7Si_8O_{22}(OH)_2$<br>*pargasite:* $Na(Ca,Mg,Fe)_2(Mg,Fe)_3(Mg,Fe)AlSi_6Al_2O_{22}(OH)_2$<br>*K-pargasite* $K(Ca,Mg,Fe)_2(Mg,Fe)_3(Mg,Fe)AlSi_6Al_2O_{22}(OH)_2$<br>*tschermakite:* $(Ca,Mg,Fe)_2(Mg,Fe)_3Al_2Si_6Al_2O_{22}(OH)_2$<br>*Ti-Fe3+ tschermakite* $(Ca,Mg,Fe)_2(Mg,Fe)_3(Ti,Fe^{3+})_2Si_6Al_2O_{22}(OH)_2$<br>*glaucophane-riebeckite:* $Na_2(Mg,Fe)_3(Al, Fe^{3+})_2Si_8O_{22}(OH)_2$ | Amp | Green et al., 2016 |
| **Pyroxenes** | | | |
| Clinopyroxene, Augite(G) | *diopside:* $CaMgSi_2O_6$<br>*hedenbergite:* $CaFeSi_2O_6$<br>*jadeite:* | Cpx | Green et al., 2016 |

| | | | |
|---|---|---|---|
| | $NaAlSi_2O_6$<br>*Ca-tschermaks:*<br>$CaAl_2SiO_6$<br>*acmite:*<br>$NaFe^{3+}Si_2O_6$ | | |
| Orthopyroxene, Opx(W) | *enstatite:*<br>$Mg_2Si_2O_6$<br>*ferrosilite:*<br>$Fe_2Si_2O_6$<br>*Mg-Fe-tschermaks:*<br>$(Mg,Fe)Al_2SiO_6$<br>*$Fe^{3+}$-tschermaks:*<br>$(Mg,Fe)Fe^{3+}AlSi_2O_6$ | Opx | White et al., 2014 |
| **Feldspars** | | | |
| K-feldspar, Kf | *microcline:*<br>$KAlSi_3O_8$<br>*albite:*<br>$NaAlSi_3O_8$ | Kfs | Thompson & Waldbaum, 1969 |
| Plagioclase, Pl(h) | *high-albite:*<br>$NaAlSi_3O_8$<br>*anorthite:*<br>$CaAl_2Si_2O_8$ | Pl | Newton et al., 1980 |
| feldspar | *anorthite:*<br>$CaAl_2Si_2O_8$<br>*microcline:*<br>$KAlSi_3O_8$<br>*high-albite:*<br>$NaAlSi_3O_8$ | Fsp | Fuhrman and Lindsley, 1988 |
| **Phyllosilicates** | | | |
| Chlorite, Chl(W) | *clinochlore:*<br>$Mg_5Al_2Si_3O_{10}(OH)_8$<br>*daphnite:*<br>$Fe_5Al_2Si_3O_{10}(OH)_8$<br>*amesite:*<br>$Mg_4Al_4Si_2O_{10}(OH)_8$<br>*Al-free-chlorite:*<br>$Mg_6Si_4O_{10}(OH)_8$ | Chl | White et al., 2014 |
| Biotite, Bio(TCC) | *annite:*<br>$KFe_3AlSi_3O_{10}(OH)_2$<br>*phlogopite:*<br>$KMg_3AlSi_3O_{10}(OH)_2$<br>*eastonite:*<br>$KMg_2Al_3Si_2O_{10}(OH)_2$<br>*ferric-biotite:*<br>$KMg_2Fe^{3+}Al_2Si_2O_{10}(OH)_2$<br>*titanium-biotite:*<br>$KMg_2TiAlSi_3O_{10}(O)_2$<br>*ordered biotite:*<br>$KMg_2FeAlSi_3O_{10}(OH)_2$ | Bt | Tajčmanová et al., 2009 |

| | | | |
|---|---|---|---|
| White mica, Mica (W) | *margarite:* $CaAl_4Si_2O_{10}(OH)_2$<br>*muscovite:* $KAl_3Si_3O_{10}(OH)_2$<br>*paragonite:* $NaAl_3Si_3O_{10}(OH)_2$<br>*celadonite:* $K(Fe,Mg)AlSi_4O_{10}(OH)_2$ | Ms | White et al., 2014 |
| Talc, T | *talc:* $Mg_3Si_4O_{10}(OH)_2$<br>*Fe-talc:* $Fe_3Si_4O_{10}(OH)_2$<br>*talc-tschermaks:* $Mg_2Al_2Si_3O_{10}(OH)_2$ | Tlc | ideal |
| **Other silicates** | | | |
| Epidote, Ep (HP11) | *Fe-epidote:* $Ca_2Fe_2AlSi_3O_{12}(OH)$<br>*clinozoisite:* $Ca_2Al_3Si_3O_{12}(OH)$ | Ep | Holland and Powell, 2011 |
| Olivine, O(HP) | *forsterite:* $Mg_2SiO_4$<br>*fayalite:* $Fe_2SiO_4$ | Ol | Holland and Powell, 1996; 1998 |
| titanite (sphene) | $CaTiSiO_5$ | ttn | pure |
| quartz | $SiO_2$ | qz | pure |
| nepheline | $NaAlSiO_4$ | nph | pure |
| leucite | $KAlSi_2O_6$ | lct | pure |
| andalusite | $Al_2SiO_5$ | and | pure |
| cordierite | $Mg_2Al_4Si_5O_{18}$ | crd | pure |
| **Carbonates** | | | |
| Dolomite, Do(HP) | *dolomite* $CaMg(CO_3)_2$<br>*ankerite* $CaFe(CO_3)_2$ | Dol | Holland and Powell, 1998 |
| Magnesite, M(HP) | *magnesite* $MgCO_3$<br>*siderite* $FeCO_3$ | Mgs | Holland and Powell, 1998 |
| calcite | $CaCO_3$ | pure | cal |
| **Oxides** | | | |
| Spinel, Sp(WPC) | *spinel:* $MgAl_2O_4$<br>*hercynite:* $FeAl_2O_4$ | Spl | White et al., 2002 |

| | | | |
|---|---|---|---|
| | *ulvöspinel:* $Fe_2TiO_4$ *magnetite:* $Fe_3O_4$ | | |
| Ilmenite, Ilm(WPH) | *ilmenite:* $FeTiO_3$ *hematite* $Fe_2O_3$ *geikielite:* $MgTiO_3$ | Ilm | White et al., 2000 |
| hematite | $Fe_2O_3$ | hem | pure |
| magnetite | $Fe_3O_4$ | mag | pure |
| rutile | $TiO_2$ | rt | pure |
| **Sulfides/sulfates** | | | |
| pyrite | $FeS_2$ | py | pure |
| Pyrrhotite, Po(HP) | *troilite* FeS $Fe_{0.88}S$ | Po | Holland and Powell, 1998 |
| anhydrite | $CaSO_4$ | anh | pure |

892

893

894

895 **Table 2:** Whole-rock starting compositions: basalt, alkali basalt, granite. Oxides are normalized

896 to 100 by Perple_X.

897

| | Basalt[1] | Alkali Basalt[2] | Granite[3] |
|---|---|---|---|
| wt. % | | | |
| $SiO_2$ | 48.7 | 47.9 | 71.4 |
| $TiO_2$ | 1.3 | 2.8 | 0.25 |
| $Al_2O_3$ | 17.9 | 18.00 | 12.38 |
| FeO | 8.8 | 9.6 | 4.59 |
| MgO | 8.1 | 3.3 | 0.16 |

| | | | |
|---|---|---|---|
| CaO | 10.3 | 7.7 | 0.77 |
| $Na_2O$ | 2.4 | 6.0 | 4.46 |
| $K_2O$ | 0.2 | 2.7 | 4.28 |

References

[1] Treiman, 2007; Filiberto, 2014

[2] Skjelkvåle et al., 1989

[3] Auwera et al., 2003

898

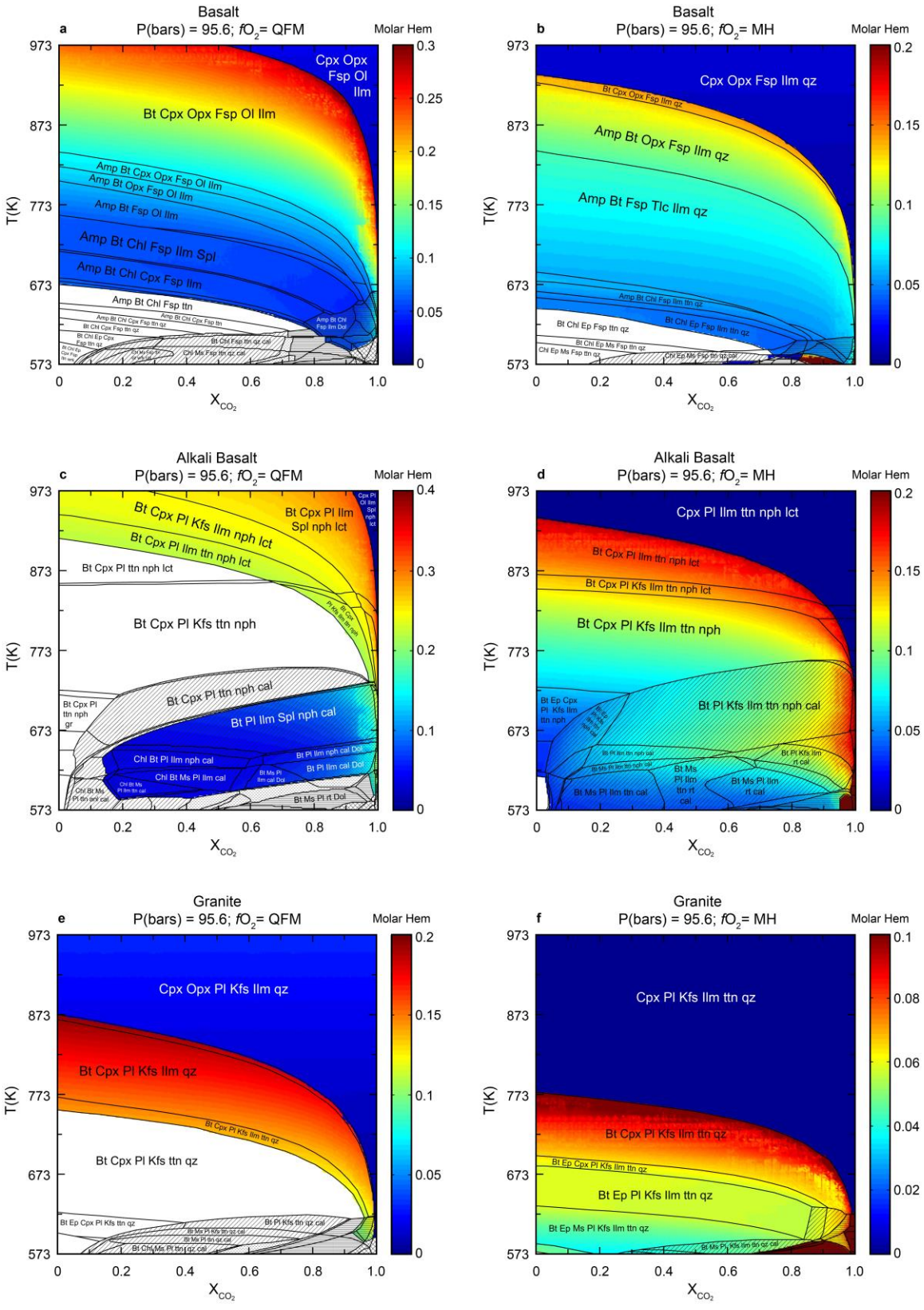
Basalt
a
P(bars) = 95.6; fO2= QFM
Molar Hem
Cpx Opx Fsp Ol Ilm
Bt Cpx Opx Fsp Ol Ilm
Amp Bt Cpx Opx Fsp Ol Ilm
Amp Bt Opx Fsp Ol Ilm
Amp Bt Fsp Ol Ilm
Amp Bt Chl Fsp Ilm Spl
Amp Bt Chl Cpx Fsp Ilm
Amp Bt Chl Fsp ttn
T(K)
XCO2
Basalt
b
P(bars) = 95.6; fO2= MH
Molar Hem
Cpx Opx Fsp Ilm qz
Amp Bt Opx Fsp Ilm qz
Amp Bt Fsp Tlc Ilm qz
Bt Chl Ep Fsp ttn qz
Bt Chl Ep Fsp Ilm ttn qz
Alkali Basalt
c
P(bars) = 95.6; fO2= QFM
Molar Hem
Bt Cpx Pl Kfs Ilm nph lct
Bt Cpx Pl Ilm ttn nph lct
Bt Cpx Pl Ilm Spl nph lct
Bt Cpx Pl ttn nph lct
Bt Cpx Pl Kfs ttn nph
Bt Cpx Pl ttn nph cal
Bt Pl Ilm Spl nph cal
Alkali Basalt
d
P(bars) = 95.6; fO2= MH
Molar Hem
Cpx Pl Ilm ttn nph lct
Bt Cpx Pl Ilm ttn nph lct
Bt Cpx Pl Kfs Ilm ttn nph lct
Bt Cpx Pl Kfs Ilm ttn nph
Bt Pl Kfs Ilm ttn nph cal
Granite
e
P(bars) = 95.6; fO2= QFM
Molar Hem
Cpx Opx Pl Kfs Ilm qz
Bt Cpx Pl Kfs Ilm qz
Bt Cpx Pl Kfs ttn qz
Granite
f
P(bars) = 95.6; fO2= MH
Molar Hem
Cpx Pl Kfs Ilm ttn qz
Bt Cpx Pl Kfs Ilm ttn qz
Bt Ep Pl Kfs Ilm ttn qz
Bt Ep Ms Pl Kfs Ilm ttn qz

899

**Figure 1:** Modeled mineral phases as a function of fluid composition ($X_{CO_2}$) and temperatures at 95.6 bars for the three protoliths (whole-rock compositions in Table 2) using the quartz-fayalite-magnetite (QFM; a, c, e) and magnetite-hematite (MH; b, d, f) buffers. Color coding represents the proportion of hematite in the hematite-ilmenite solid solution (abbreviated as Ilm), which varies with protolith and oxygen buffers. Textures represent the following: calcite – diagonal lines; calcite + dolomite – dashed lines; dolomite – solid lines; dolomite + magnesite – diamonds. Mineral abbreviations are listed in Table 1.

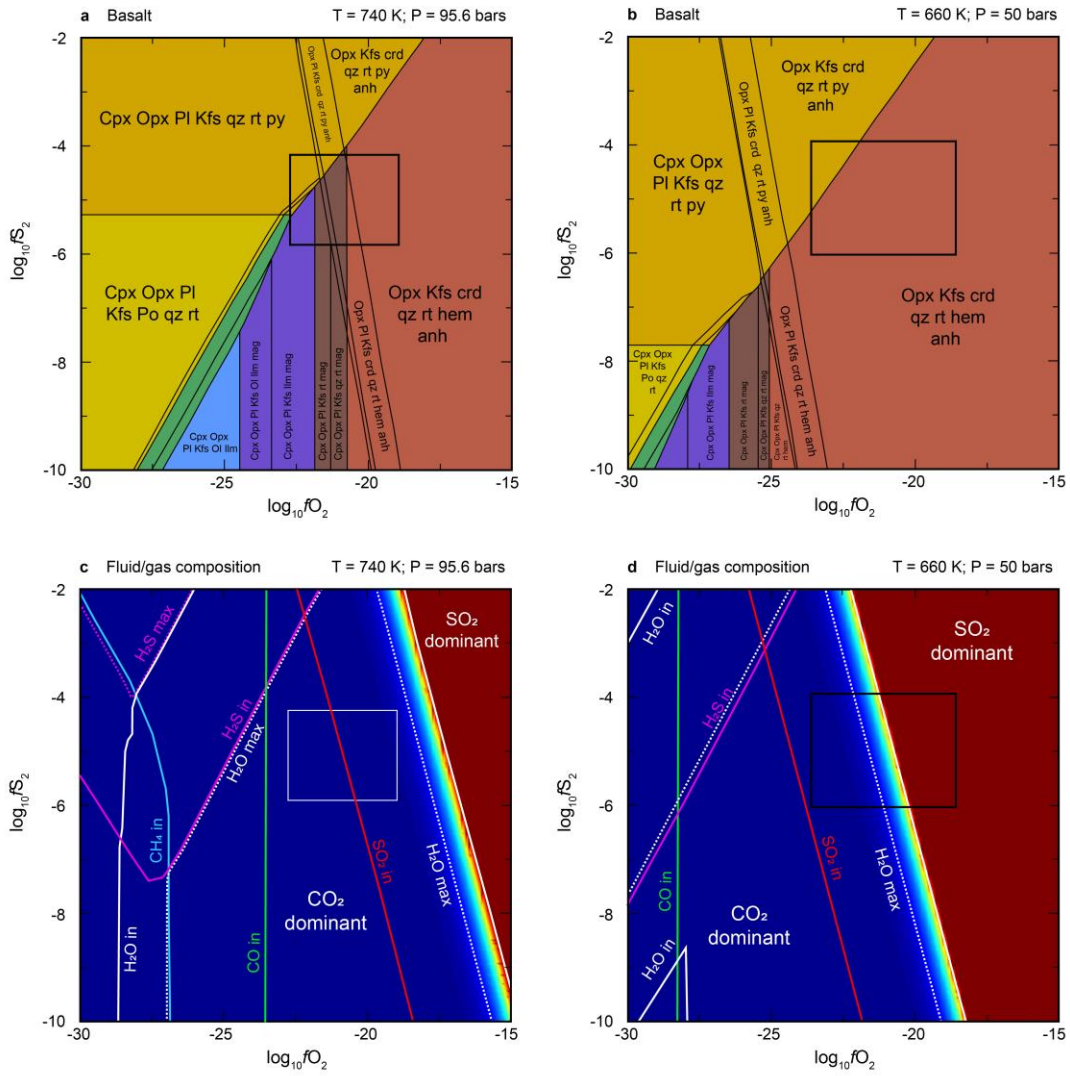


**Figure 2:** Phase equilibria for the basalt composition as a function of oxygen and sulfur fugacities and at temperature-pressure conditions relevant for planetary radius (740K, 95.6 bars; a) and high elevations (660 K, 50 bars; b). The black boxes represent fugacities that are most likely expected at planetary radius and at higher elevation, including larger uncertainties. Hematite – red, magnetite – brown, pyrite – dark yellow, pyrrhotite – bright yellow, ilmenite + magnetite – purple, ilmenite – blue, ilmenite + pyrrhotite – green. The composition of the gas in equilibrium with the solid phase is shown in c) and d). Solid lines represent the minimum amount of the species, while dashed lines represent the maximum amount. $H_2$ not shown due to limited stability.

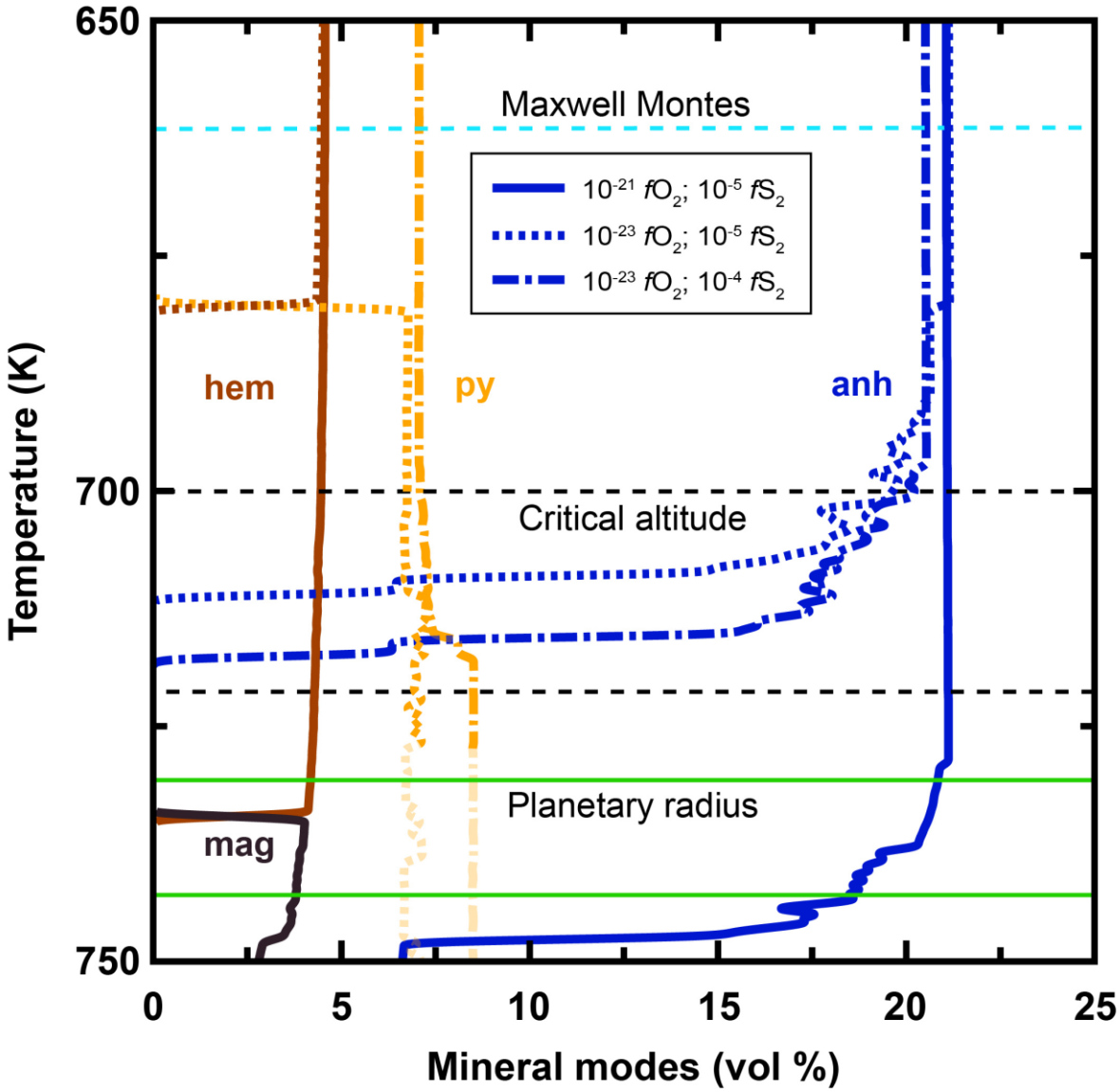


**Figure 3:** Modeled abundance of Fe-, and S-bearing minerals as a function of temperature at three different oxygen- and sulfur fugacities for the basaltic protolith. Temperature conditions at modal planetary radius are indicated by the green box. The critical altitude (dashed black box) represents altitudes at which the emissivity drops steeply and is estimated to lie between ~ 2 km up to 5 km depending on regional differences. The dashed cyan line represents conditions at the highest altitudes on Maxwell Montes. Solid lines: mineral modes calculated for conditions of $fO_2$ = $10^{-21}$ and $fS_2$ = $10^{-5}$ relevant for modal planetary radius. If these fugacities were constant with

decreasing temperature (and therefore altitude), pyrite would not be stable. Dashed lines: mineral modes at lower oxygen fugacities than determined on Venus' surface with variations in sulfur fugacities. If fugacities change with elevation, pyrite could be a stable phase at lower temperatures and higher elevation. Pyrite is not expected to be stable at conditions relevant for the modal planetary radius, which is indicated by the faded part of the curve.

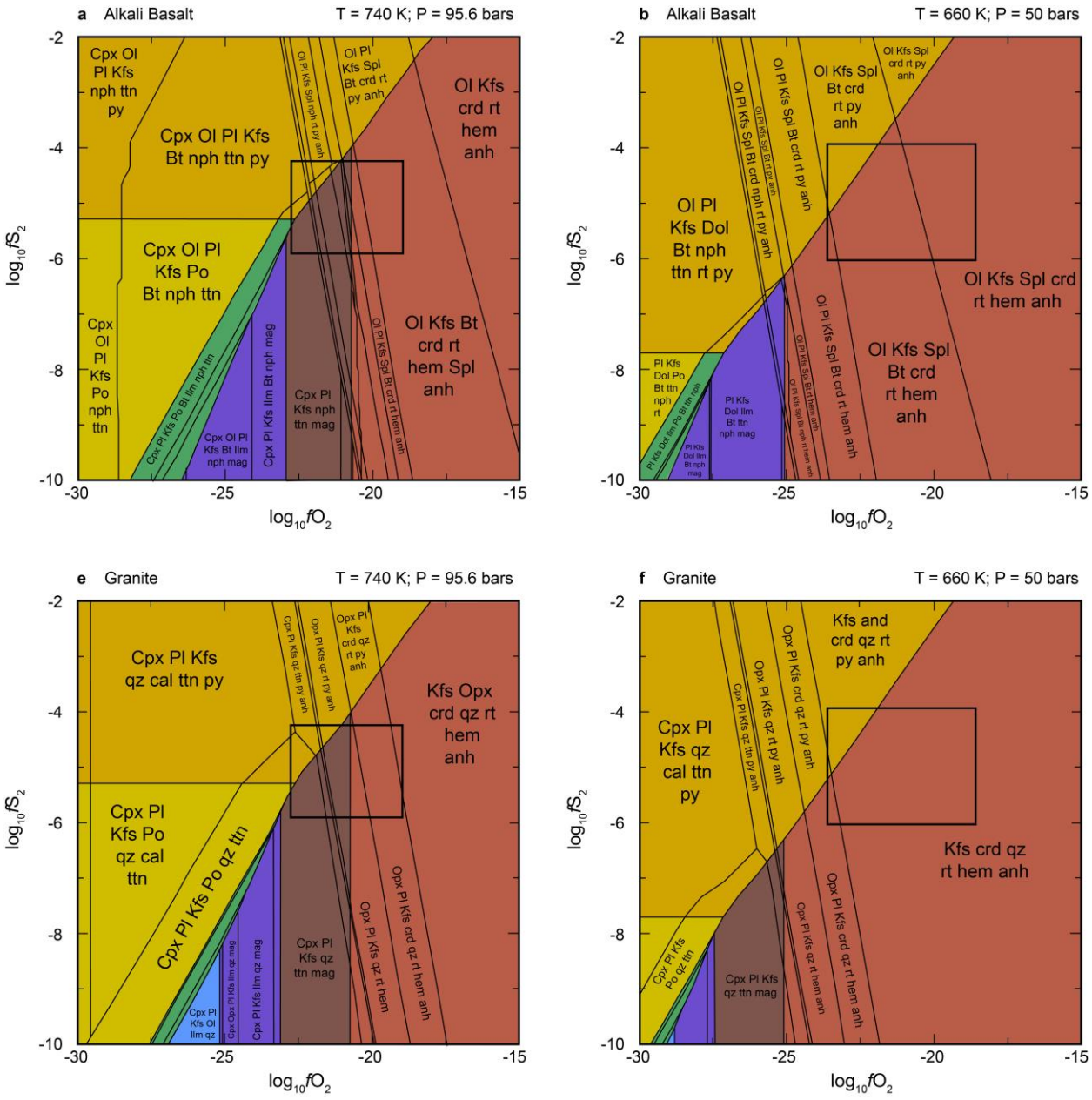


933

934

935 **Supplementary Fig. 1:** Phase equilibria for the alkali basalt (a, b) and granite (c,d) compositions
936 as a function of oxygen and sulfur fugacities and at temperature-pressure conditions relevant for
937 planetary radius (740 K, 95.6 bar; a,c) and high elevations (660 K, 50 bar; b,d). The black boxes
938 represent fugacities that are most likely expected at planetary radius and at higher elevation,

939 including larger uncertainties. Hematite – red, magnetite – brown, pyrite – dark yellow, pyrrhotite
940 – bright yellow, ilmenite + magnetite – purple, ilmenite – blue, ilmenite + pyrrhotite – green.